Available online at www.sciencedirect.com
SCIENCE DIRECT®
International Journal of Mass Spectrometry 228 (2003) 237–267
International Journal of Mass Spectrometry
www.elsevier.com/locate/ijms

# Theory, simulation and measurement of chemical mass shifts in RF quadrupole ion traps

Wolfgang R. Plass[1], Hongyan Li, R. Graham Cooks*

*Department of Chemistry, Purdue University, West Lafayette, IN 47907-1393, USA*

Received 5 December 2002; accepted 17 March 2003

**Abstract**

A comprehensive description of chemical mass shifts in the RF quadrupole ion trap (Paul trap) is given and their origin is explained. Extending a previously proposed model, it is shown that chemical mass shifts are a result of an ejection delay caused by field imperfections in RF ion traps with non-optimized geometry, in particular, field imperfections resulting from holes in the end-cap electrodes, and of compound-dependent modifications of this ejection delay by collisions of the ions with the buffer gas. Elastic collisions change peak shapes and peak widths, but give rise to only very small chemical mass shifts. Inelastic collisions, which result in dissociation, can lead to large chemical mass shifts. The field imperfections present in real ion traps are examined, and differences in the ion ejection behavior and in the chemical mass shifts occurring in boundary ejection and resonance ejection scans are investigated. The dependence of the shifts on the trap geometry, on the buffer gas pressure, on the RF amplitude scan rate, on ion mass, and on ion chemical structure, are explained. The proposed model for chemical mass shifts is validated through experimental measurements and quantitative simulations using the ion trap simulation program ITSIM. It is shown that peak shapes in mass spectra can be reproduced or predicted by simulations, for ion traps with a variety of geometries and operating conditions. Very good agreement between simulations and experiments is found, provided experimental and simulated geometries differ slightly in the end-cap separation, indicating that additional previously neglected field imperfections may be present in common RF ion traps.
© 2003 Elsevier Science B.V. All rights reserved.

*Keywords:* Chemical mass shift; RF quadrupole ion trap; Nonlinear fields; Simulation; Ion motion

## 1. Introduction

In RF ion traps, mass analysis is usually performed using the mass-selective instability scan. This was done originally by scanning the working points of the ions through the boundary of the stability diagram in the order of the ion's mass, and thus ejecting them from the trap into an external detector [1,2]. The boundary ejection method was later replaced by resonance ejection, a method according to which the working points of the ions are scanned through a resonance line created by application of a supplementary AC voltage [3,4]. Particular strengths of RF ion traps include its high sensitivity [1,5–7] and capabilities for multi-stage mass spectrometry [8–10].

* Corresponding author. Tel.: +1-765-494-5263; fax: +1-765-494-9421.
*E-mail address:* cooks@purdue.edu (R.G. Cooks).
[1] On-leave from and present address: II. Physikalisches Institut, Justus-Liebig Universität Giessen, Heinrich-Buff-Ring 16, 35392 Giessen, Germany. Part of doctoral thesis.

1387-3806/$ – see front matter © 2003 Elsevier Science B.V. All rights reserved.
doi:10.1016/S1387-3806(03)00216-1

Commercial ion trap instruments are typically limited to a mass-to-charge accuracy of 0.1 Th up to a mass-to-charge ratio of 2000 Th (the unit Thomson is defined as 1 Th = 1 u/$e_0$, where u is the atomic mass unit and $e_0$ the elementary charge [11]). The best values reported are 10–40 ppm [12,13]. Factors that limit the accuracy of RF ion traps have been summarized in a recent study [13]. They include the stability of the RF voltage and the resonance ejection voltage, the stability of the buffer gas pressure, and space charge effects. The last factor results in delayed ejection for all ions, but the exact ejection time, and hence apparent mass-to-charge ratio is also dependent on the masses of the ions present in the trap and their relative abundances. Space charge effects are usually reduced by limiting the number of ions in the trap, although extrapolation to zero ion abundance [14] and translational excitation in multiple dimensions [15] have also been proposed as means of eliminating space charge effects. Mass measurement errors that occur for ions of similar mass but different structure and that are related to field imperfections have been recognized as the major factor influencing performance. They can be as large as 1000 ppm [13].

These mass mis-assignments are termed mass shifts, compound-dependent mass shifts or chemical mass shifts in the literature and will be referred here as chemical mass shifts. Since mass analysis in RF ion traps is affected by measuring the mass-to-charge ratio, the terms mass shifts and mass-to-charge shifts will be used interchangeably. Chemical mass shifts in the mass-selective instability scan were first observed and carefully studied by Stafford et al. at Finnigan in 1984 during the commercialization of the RF ion trap [16]. Stafford and coworkers found that the masses for some ions, e.g., nitrobenzene and pyrene, were assigned incorrectly, while for the majority of the ions—within the limits set by the mass resolution—the correct mass-to-charge ratio was measured. The observed shifts were as large as 0.7 Th. The problem was solved empirically by changing the distance $z_0$ between the center of the trap and the tips of the end-cap electrodes from the original value of 7.07 mm to 7.83 mm. The value $z_0$ = 7.07 mm (theoretical geometry) was chosen originally as the value predicted by theory [17] to create a purely quadrupolar field for a trap with an inner radius of the ring electrode of $r_0$ = 10 mm. The change to $z_0$ = 7.83 mm (commercial geometry) was made without a corresponding change in the shape of the hyperbolic shape of the electrodes, and it therefore added higher order field components to the trapping field. To date, all commercial RF ion trap mass spectrometers use a geometry that differs from the theoretically ideal case. In Bruker ion trap mass spectrometers, a modified hyperbolic angle is used [18]. Recent advances in the mass resolution of RF ion traps show that chemical mass shifts are not completely eliminated by these procedures. Certain fragile ions undergo small chemical mass shifts even in commercial ion trap mass spectrometers [19–21]. In contrast, the large chemical mass shifts reported here arise only in those RF ion traps whose geometry has been changed significantly from the commercial geometry.

Recently, a model was developed that explains the occurrence of chemical mass shifts [22–24]. According to this model, holes in the end-cap electrodes cause field imperfections that give rise to a prolonged delay in ion ejection in the mass-selective instability scan, whether performed with or without resonance ejection. While this delay arises for any ion species, it is modified in a compound-dependent fashion by elastic and dissociative collisions. The deliberate introduction of additional field imperfections by increasing the end-cap separation compensates for the effect of the end-cap holes and effectively removes the ejection delay. In this paper, this model for chemical mass shifts is expanded and described in depth, and further experimental and simulation results are presented to validate the model.

## 2. Experimental

Experiments were conducted using two Finnigan ion traps (Thermo Finnigan, San Jose, CA), a modified Finnigan ITMS ion trap mass spectrometer and a modified Finnigan GCQ ion trap mass spectrometer. The Finnigan ITMS included a custom-designed

mechanical system [25] which was used to change the end-cap spacing under operating conditions during the course of a series of experiments. The accuracy of the positioning, verified twice using measuring blocks, is estimated as 0.1 mm. Pressure was measured using a Bayert–Alpert ionization gauge with a Granville-Phillips 307 vacuum controller (Granville-Phillips, Boulder, CO). The nominal background pressure was $6 \times 10^{-7}$ Torr. Organic samples were degassed using several freeze–pump–thaw cycles and introduced into the vacuum system using a Granville-Phillips variable-leak valve to a nominal pressure of $9 \times 10^{-7}$ Torr. Helium was used as buffer gas at different pressures; the values reported have been corrected for ion gauge sensitivity [26]. The Finnigan ITMS uses an RF frequency of 1.1 MHz and a nominal scan speed of 5.555 Th/ms. Each mass scan was preceded by internal electron ionization for a selected time at a low-mass cut-off (LMCO) [27] of 40 Th, followed by a 5 ms cooling period, selection of the ion of interest by RF/DC isolation at the upper apex of the Mathieu stability diagram, and 5 ms cooling time at a LMCO of 40 Th after isolation. The dynode/electron multiplier system was operated at −5 and 1.9 kV, respectively. A Tektronix TDS 540 digitizing oscilloscope (Tektronix, Beaverton, OR) was used to acquire the signals produced by the preamplifier as a function of ion ejection time at a sampling rate of 250 ksamples/s with 100 scans being averaged for each spectrum. Space charge effects were minimized by controlling the ionization time using the following procedure: in an initial study, the ionization time was varied and the ion abundance was determined by measuring the peak area of the selected ions on the oscilloscope. The shifts in ejection time caused by changes in the ion abundance were monitored. With decreasing ion abundance, the ejection times converge towards a constant value. A target value for the peak area was chosen, so as to make the space charge shifts negligible. In all subsequent experiments, the ionization times were adjusted such that the measured peak area matched this target value.

The Finnigan GCQ ion trap mass spectrometer was modified from the commercial geometry by replacing the electrode spacers. The center–end-cap spacing was changed from that of the commercial geometry $z_0 = 7.83$ mm to that of the theoretical geometry $z_0 = 7.07$ mm. The normal instrument control and data acquisition hardware was replaced with the instrument control and data acquisition module of a Finnigan LCQ ion trap mass spectrometer. This module allows the Finnigan GCQ to be controlled with Finnigan's proprietary Ion Trap Control Language (ITCL), which contains commands to freely change the instrument voltages and scan functions. The Finnigan GCQ uses an RF frequency of 1.03 MHz and a nominal scan speed in the commercial geometry of 11.11 Th/ms. Samples were introduced into the external GCQ electron impact ion source through a GC oven using a 30 m, 250-μm inner diameter deactivated column. The temperature of the ion source was set to 200 °C. The GC oven was set at different temperatures, depending on the volatility of the sample. The instrument's Automatic Gain Control was used to keep the number of ions in the trap constant by changing the ion injection time. For each mass spectrum 1000 scans were averaged.

Two different methods were employed for converting the measured ejection times into mass-to-charge ratios. In the first calibration method, the 69, 100, and 131 u fragment ions of perfluoro-tri-*n*-butylamine (PFTBA) were used as calibrant ions. Their ejection times were measured from the positions of the peak maxima. The mass calibration relationship was then established by a linear fit of the ejection times of the calibrant ions vs. their exact masses. All results that give the chemical mass shift $\Delta(m/e)$ were calculated using this calibration method. Chemical mass shifts are reported as the true mass of the ion minus the measured mass, hence ions that are ejected early are assigned a positive chemical mass shift. The standard deviation in the measurement of the chemical mass shifts was 0.05 Th. This calibration method is easy to perform, but it has the disadvantage that it is influenced by changes in the ejection time of the calibrant ions themselves. Therefore, a second calibration method was used to permit the investigation of the apparent mass-to-charge ratio of the ions as a function of the operating conditions independently of the behavior of

calibrant ions. In this method, the ejection time of the ion of interest was determined from the position of the peak center. For conversion to mass-to-charge ratio, the RF amplitude was measured using a Tektronix P6015 1000× high voltage probe. From the instrumental parameters, the mass-to-charge ratios of the ions of interest were then calculated using the mass analysis equation

$$\left(\frac{m}{e}\right) = -\frac{4A_2^{\mathrm{R}}}{q_{\mathrm{ej}} r_{\mathrm{N}}^2 \Omega^2} V(t_{\mathrm{ej}}) \quad (1)$$

where $t_{\mathrm{ej}}$ is the ion ejection time, $q_{\mathrm{ej}}$ is the Mathieu parameter corresponding to the ejection point, $A_2^{\mathrm{R}}$ is the quadrupole expansion coefficient describing the strength of the quadrupole field, and $r_{\mathrm{N}}$ the normalization radius (see below), $\Omega/(2\pi)$ is the RF frequency, $m$ and $e$ the ion mass and charge, respectively. The RF amplitude $V$ is increased linearly with time $t$ such that,

$$V(t) = At + V_0 \quad (2)$$

Note that in this mass calibration procedure, the apparent mass is equal to the true mass if the ion is ejected immediately at the onset of instability in the central region of the trap in the absence of collisions and space charge effects. A delay in ion ejection results in a higher apparent mass. The effects of non-ideal conditions can, therefore, be detected easily as a shift in the apparent mass. All results that specify the apparent mass-to-charge ratio $(m/e)_{\mathrm{ap}}$ or the relative apparent mass-to-charge, i.e., the ratio $(m/e)_{\mathrm{ap}}/(m/e)$, were calculated using this calibration method.

## 3. Simulation software and settings

Simulations were performed using the ion trap simulation program ITSIM 5.0 [28,29]. For qualitative simulations, single ion trajectories were calculated using the initial conditions given in the corresponding figures. In the quantitative simulations, the mass-selective instability scan was simulated using $10^4$ ions. In order to reduce the computation time, the full scan starting from a LMCO of 40 Th was simulated once for 1000 ions of each ionic species and for four different helium buffer gas pressures each. All subsequent simulations using $10^4$ ions were started from the working point $q_z = 0.85$, $a_z = 0$. The initial conditions for these simulations, i.e., the initial ion cloud dimensions, were chosen to match the values obtained for this working point in the preliminary simulations.

A numerical field interpolation method was used to calculate the electric field inside the trap from a two-dimensional array of electric potential values on a rectangular grid with a grid point distance of 0.02 mm. The electric field strength at each grid point was obtained as a centered difference from the potential at neighboring grid points, and the field at intermediate positions was calculated from the field on the grid points by bilinear interpolation. The electric potential was pre-calculated using the POISSON/SUPERFISH software [30]. The six holes positioned on a circle around the central hole in the Finnigan ITMS exit end-cap electrode were modeled by an annulus with a thickness of 0.8 mm, which creates approximately the same electric field as the six end-cap holes, while maintaining rotational symmetry. A fourth-order Runge–Kutta method with a step size of 5 ns was used to integrate the equation of motion.

Collisions were modeled using velocity-dependent collision cross-sections taken from the literature [31,32] or calculated using a projection method [28,33]. Inelastic collisions were treated by considering stepwise changes in ion internal energy, taking into account microscopic reversibility and conservation of momentum and energy. The average amount of energy transferred between translational and internal degrees of freedom is determined in this model [29,34] by the collision energy, the density of states of the ion, the ion internal energy and the internal energy up-step efficiency, which gives the fraction of center-of-mass (COM) energy converted to internal energy in collisions that lead to excitation. The internal energy up-step efficiency is treated as a parameter which can be adjusted to match the experimentally observed inelastic collision properties. The amount of energy transferred in de-excitation collisions is determined from the conditions for excitation collisions by microscopic reversibility. Dissociation was modeled

using RRKM theory [35]. The vibrational frequencies of *n*-butylbenzene were taken from literature values for the neutral molecule [36].

A comparison of the simulated and measured spectra showed that peak shapes and peak widths could be reproduced very well, provided measured and simulated spectra are compared, which differ by a constant difference in the center–end-cap distance $z_0$ and by a constant factor in the helium buffer gas pressure, and used slightly different RF voltage scan rates. The small difference in RF voltage is mostly due to inaccuracies in the experimental voltage measurement. To circumvent this problem, the exact voltage scan rate appropriate for the conversion of the experimentally measured times to mass-to-charge ratio was determined once by a comparison of the simulated and measured mass peak of the 131 u fragment of the mass reference compound, PFTBA, at $z_0 = 8.0$ mm, rather than by using the measured voltage scan rate. The choice of $z_0$ for this comparison will be validated below. The RF scan rate obtained by the comparison of the measured and the simulated mass peak deviates by 4% from the experimentally measured scan rate, which is as large as the estimated error of the voltage measurement. However, the difference also includes a possible deviation between the (not exactly known) real geometry and the modeled geometry. Such a deviation results in different quadrupolar field strengths, just as a difference in the applied voltage does. Hence, ejection times will be different in different geometries, even if the effects of higher order fields are ignored. Conversely, any voltage calibration based on a comparison of ejection times includes differences in the geometries. The voltage scan rate, thus obtained, was used to convert the measured and the simulated ejection times to the theoretically expected mass, as given by the mass analysis Eq. (1). The helium buffer gas pressure in the experiments must be larger by a factor of two than the pressure in the matching simulations. This effect is most likely due to the inaccuracy in the experimental pressure measurements. Drift tube simulations obtained with ITSIM give results that differ from experiments and analytical solutions by not more than 20% [29]. Consistency between the experiments and simulations required that experimental spectra be taken using a center–end-cap separation $z_0$ which is larger by 0.3 mm than the matching simulated spectra. The implications of this difference in $z_0$ will be discussed below.

It should be emphasized that the corrections in voltage scan rate, $z_0$, and helium buffer gas pressure were determined only once and are used consistently for all simulations. In all cases, the actual $z_0$ values and pressure values are given, and the corrections are used only to select the spectra which are compared with each other.

## 4. Theory

### 4.1. Ion motion in linear and nonlinear fields

The electric potential in an RF trap with Azimuthal symmetry can be expressed in terms of a multipole expansion, which in spherical coordinates $(r, \vartheta, \varphi)$ takes the form

$$\Phi(\rho, \vartheta, \varphi, t) = \sum_n \Phi^{(n)}(t) \sum_{l=0}^{\infty} A_l^{(n)} \left(\frac{\rho}{r_N}\right)^l P_l(\cos\vartheta) \tag{3}$$

The sum over $n$ includes all electrodes of the trap, $\Phi^{(n)}(t)$ is the potential on the $n$-th electrode and may be explicitly time dependent, $r_N$ is a normalization radius, $A_l^{(n)}$ are the corresponding dimensionless expansion coefficients, and $P_l(\cos\vartheta)$ is the Legendre polynomial of order $l$ [37]. Only the expansion coefficients for the ring electrode are of interest here; for consistency with previous work [38] they are designated with the superscript 'R'.

In an ideal ion trap operated with grounded end-cap electrodes and a voltage applied to the ring electrode, only the quadrupole term ($l = 2$) of the ring electrode contributes to the electric field. In such a quadrupolar field, the magnitude of the field strength increases linearly with distance from the trap center. The ion motion in the radial ($r$) and axial ($z$) directions is uncoupled and described by the solutions of the Mathieu equation [39]. The motion is either purely oscillatory

(stable motion) or it includes a term with exponentially increasing amplitude (unstable motion). In the first case the ion is usually trapped, in the latter case the ion leaves the trap. Whether motional stability or instability applies is determined by the operating conditions and the mass-to-charge ratio of the ions. Mass analysis is performed by increasing the RF amplitude with time, bringing the ions in the order of their mass-to-charge ratios to working points of motional instability (mass-selective instability scan with boundary ejection) or into resonance with a supplementary AC voltage (mass-selective instability scan with resonance ejection), thus ejecting them from the trap into a detector. In both modes of operation a light buffer gas, usually helium, is employed to collisionally cool the ion cloud before the mass scan. Ion motion in linear fields has the important property that the oscillation frequencies and the stability of ion motion are independent of the oscillation amplitude, viz. of the initial conditions. Hence, the mass measurement depends only weakly on the position of the ions in the trap, and resonance phenomena are position independent.

Ion traps in which there is a small proportion of higher order fields superimposed on the linear field, i.e., fields whose magnitude increases more strongly than linearly with distance from the center of the trap, are commonly referred to as nonlinear traps [40]. Their multipole expansion includes terms with $l > 2$. Of practical importance are the hexapole term ($l = 3$), the octopole term ($l = 4$), and the dodecapole term ($l = 6$). Real ion traps always include nonlinear fields that arise from the deviation of the electrode geometry from the ideal shape. The sign of a higher order field term is defined as positive if it adds to the absolute value of the quadrupole field on the axis of symmetry, i.e., if the relative multipole weight $A_l^R/A_2^R$ is positive, and as negative otherwise [40].

Nonlinear fields give rise to the following effects in RF ion traps: (i) The ion oscillation frequencies are shifted from the value for purely linear fields. The frequency is position dependent, and the magnitude of the frequency shift increases with oscillation amplitude. In a field whose magnitude increases more strongly than linearly with distance from the trap center, the ion experiences, on average, a higher field strength as its oscillation amplitude is increased. Thus, the axial oscillation frequency increases with oscillation amplitude for fields with superimposed higher order multipoles which are even and positive in sign. Conversely, it decreases with oscillation amplitude for fields with corresponding negative higher order multipoles. Odd higher order multipoles do not shift the oscillation frequency to a first approximation, because the higher order field superposition adds to the field strength on one side of the center of the trap and subtracts from the field on the other side [40]. The frequency shifts caused by nonlinear fields are usually small (of the order of 1% or less). However, they can have serious consequences for the operation of RF ion traps [40–42]. Of particular importance is the amplitude-dependent shift of the oscillation frequency caused by nonlinear fields for ion ejection during the mass-selective instability scan. (ii) For certain working points in the stability diagram, nonlinear resonances can occur in nonlinear ion traps, which lead to energy pickup of the ion from the RF field and possibly to ejection of the ion from the trap even without application of supplementary fields [40,43,44]. (iii) Higher order fields cause a coupling between axial and radial motion. This effect, however, is small during typical ion trap operation.

### 4.2. Fields in real ion traps

It is instructive to consider the differences between the electric fields in ideal traps of theoretical geometry ($r_0 = 10\,\text{mm}$, $z_0 = 7.07\,\text{mm}$), and those in the commercial geometry ($r_0 = 10\,\text{mm}$, $z_0 = 7.83\,\text{mm}$) for Finnigan ITD and ITMS ion trap mass spectrometers. Fig. 1 shows the relative multipole weights $A_l^R/A_2^R$ as a function of the ratio $z_0/r_0$ of the distance between the center of the ion trap and the tips of the end-cap electrodes $z_0$ and the inner radius of the ring electrode $r_0$ calculated for an ideal trap using a multipole expansion fitting method [29]. For the calculation, the electrodes were truncated at a distance $r_{\text{trunc}} = 2.5r_0$ from the trap center with the boundary conditions set such that the equipotential lines are parallel to the electrode asymptotes. This ensures that the effect of the

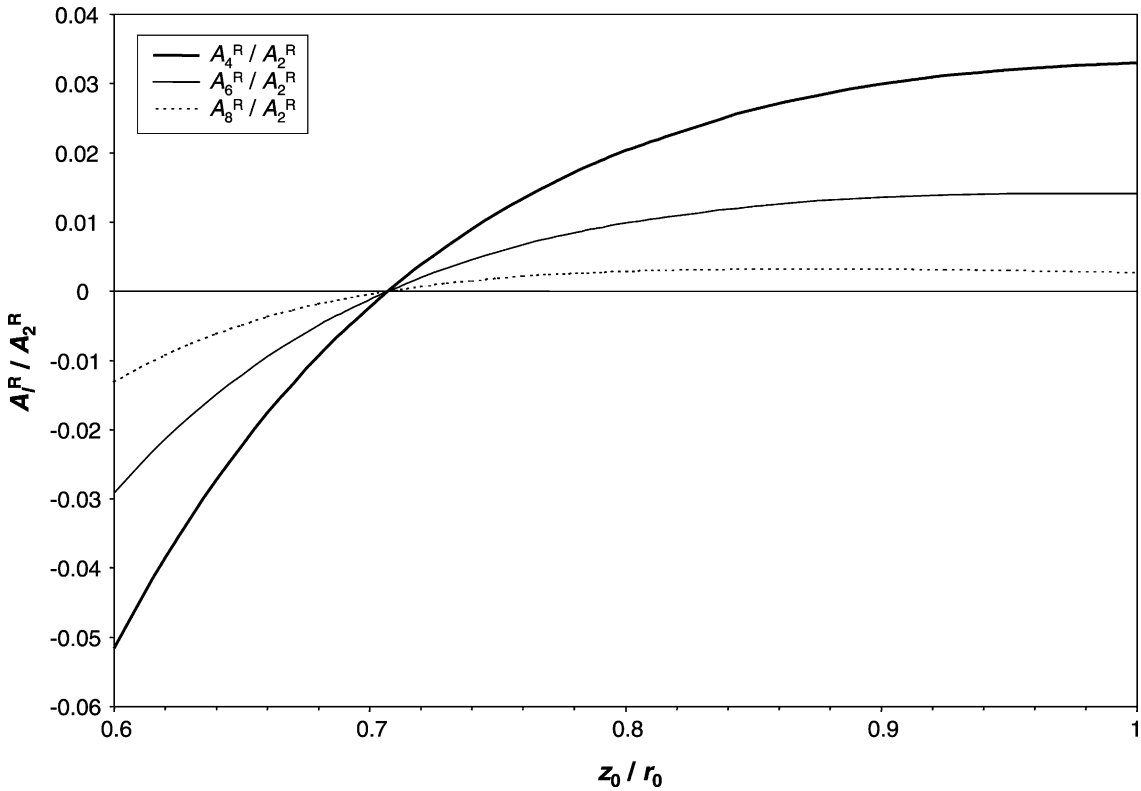


Fig. 1. Even higher order multipole weights for the Finnigan ITMS ion trap, without the effects of truncation and end-cap holes as a function of $z_0/r_0$. The multipole coefficients were calculated using a multipole expansion fitting method [29].

truncation on the electric field in the regions of interest of the trap is negligible. It can be seen that increasing the end-cap separation introduces positive higher order fields, whereas reducing the separation introduces negative higher order fields. The relative octopole weight at $z_0 = 7.83\,\text{mm}$ is about $A_4^R/A_2^R = 0.018$; the relative multipole weights of orders higher than the octopole are also positive, but smaller. It seems plausible that the best ion trap performance can be obtained in ion traps with purely linear fields, since in this case the ion oscillation frequency is independent of the oscillation amplitude and ions behave similarly, even if located at different positions. Therefore, it appears contradictory that chemical mass shifts would arise in the theoretical geometry with purely linear fields, while they would disappear in the commercial geometry with its nonlinear fields, as was observed experimentally [16,25]. This contradiction is solved if additional field imperfections can be found which necessitate the addition of positive higher order fields by increasing the end-cap separation in order to lead to a mutual compensation of the higher order fields. These negative higher order fields must be present in the original Finnigan ion trap in the theoretical geometry $z_0 = 7.07\,\text{mm}$, and cause chemical mass shifts.

It has been argued that the truncation of the electrodes to finite size introduces negative higher order fields, which are then offset by increasing the end-cap electrode spacing [40]. However, calculations show that the truncation results in higher order fields that are an order of magnitude too small to account for the required increase in $z_0$ [45]. These calculations were repeated here for the Finnigan ITD and ITMS ion traps. The geometry used for these field calculations, and

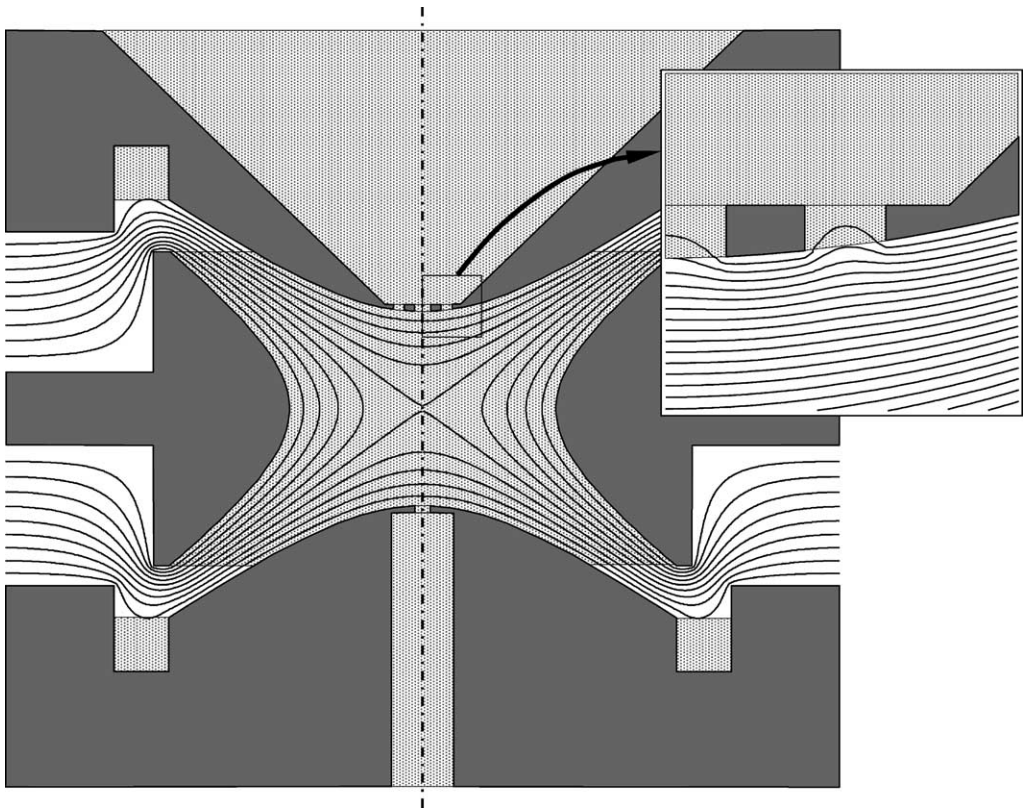

Fig. 2. Scheme of the Finnigan ITD and ITMS ion trap electrodes and the quadrupolar potential distribution, showing the effect of the holes in the end-cap electrodes and the electrode truncation.

the potential distribution in the quadrupolar mode are shown in Fig. 2. It was found that the truncation effects are negligible compared to the effects of increasing the end-cap separation. Similarly, possible machining errors have been found to be too small. Random variations in the electrode shape and mounting cannot account for the chemical mass shifts, since chemical mass shifts measured on different Finnigan ion trap mass spectrometers have similar values [22,23,46].

A source of negative higher order fields is the holes in the end-cap electrodes. In Finnigan ITD and ITMS ion traps, they have a diameter of 1.2 mm; one hole is located at the tip of each end-cap, and the exit end-cap electrode has six additional holes that are arranged on a circle around the central hole. In Fig. 2, it can be seen that the equipotential lines penetrate into the end-cap holes, thus decreasing the electric field strength in the vicinity of the end-cap holes. Laser tomography experiments conducted by Cleven et al. [47] indicate that there is a correlation between the size of the perforations in the end-caps and the chemical mass shift. This constitutes experimental evidence that the perforations are a major reason for field faults in quadrupole traps.

A quantitative investigation of the effects of the end-cap holes and the end-cap separation on the electric field is given in Fig. 3 for an ITMS ion trap in the theoretical and in the commercial geometry with a hole with a diameter of 1.2 mm in each end-cap. Here, the six additional holes in the exit end-cap have been omitted for simplicity. During the mass-selective instability scan the ions do not move far from the axis of symmetry, provided they have initially been cooled to central positions in the ion trap, and they are ejected in the axial direction. Therefore, it is sufficient to

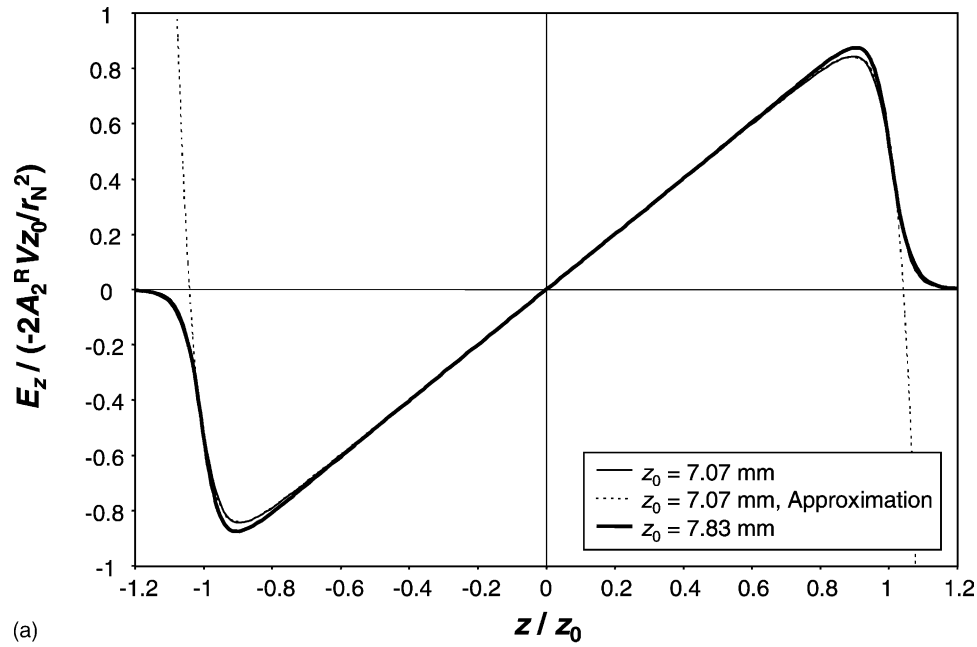


(a)

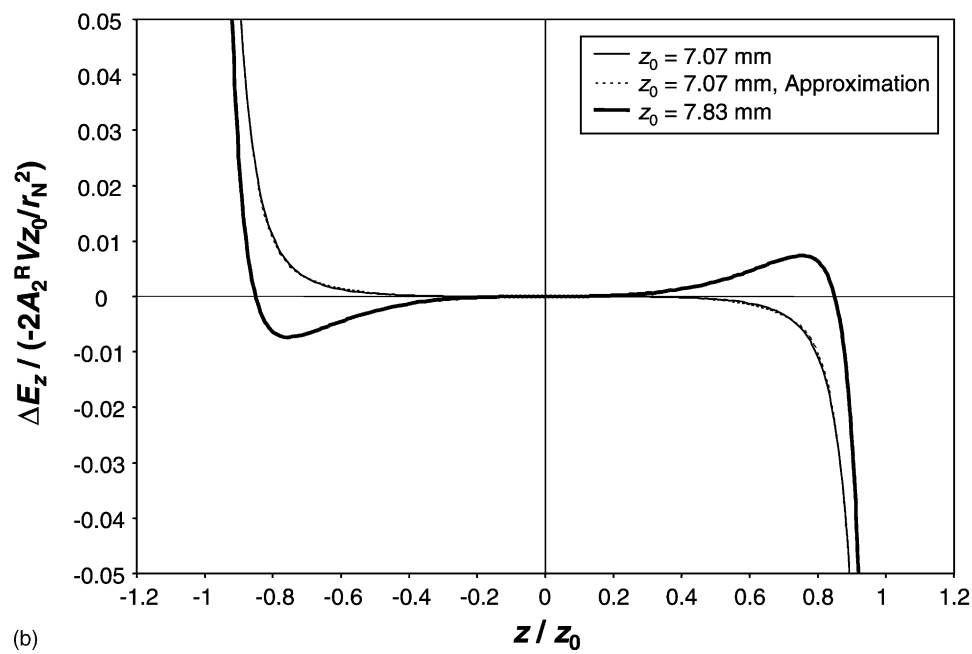


(b)

Fig. 3. (a) Axial electric field and (b) nonlinear contribution to the axial electric field on the axis of symmetry in the Finnigan ITMS ion trap in the theoretical geometry ($z_0 = 7.07$ mm) with one hole in each end-cap and in the commercial geometry ($z_0 = 7.83$ mm) with one hole in each end-cap. Up to $z = \pm z_0$ the analytical approximation for the theoretical geometry (dotted curve) almost coincides with the numerical solution.

consider the axial component of the electric field on the axis of symmetry. To allow a quantitative comparison of the two geometries, the axial dimension and the field strength have been normalized independently, correcting for the different field strengths caused by the difference in the end-cap distance. From Fig. 3a it can be seen that the axial field strength increases nearly linearly with the distance from the center of the trap. For ideal traps the field strength would increase linearly to the end-caps, and then it would abruptly go to zero. The effect of the end-cap holes is that the electric field strength drops off slowly in the vicinity of the end-cap electrodes. Simulations show that ions are ejected from the trap when they reach the axial position at which the field strength starts to decline, whereas in purely linear fields the ions are only lost when their motion takes them outside the trapping volume. The end-cap holes result in a gradual, curved drop-off in field strength which corresponds to contributions from negative higher order field components. In the commercial geometry the normalized field strength near the end-cap holes is higher than in the theoretical geometry.

This is shown more clearly in Fig. 3b, in which the linear contributions to the electric field have been subtracted and only the nonlinear axial electric field is given. In the theoretical geometry with end-cap holes, the nonlinear fields are negative. In the commercial geometry with end-cap holes, the nonlinear fields are positive for positions up to approximately $z = 0.8z_0$, but become negative close to the end-cap electrodes. It is not possible to exactly compensate for the field imperfections in the vicinity of the end-cap holes by increasing the end-cap separation, because the higher order fields introduced by both methods vary differently with distance. The increase in the end-cap separation can, therefore, only cause an effective compensation in the sense that the effects of the end-cap holes on the ion motion are minimized, and not that purely linear fields are created. The observation that the nonlinear fields in the central regions of the trap are positive is supported by resonance excitation experiments in Finnigan ITMS ion traps, which show that the resonance curve is asymmetric, with the maximum shifted towards higher excitation frequencies [41]. This is the expected shape of the resonance curve for an ion trap with a superposition of positive higher order fields.

Also shown in Fig. 3 is an analytical approximation for the electric field (dotted line). This approximation is similar, but not identical, to the multipole expansion commonly used for quadrupole ion traps. Small details in the trap geometry cannot be modeled well using the multipole expansion approach. In particular, the perforations in the end-cap electrodes cannot be approximated well by a global multipole expansion. The diameter of the holes is an order of magnitude smaller than the end-cap separation, hence the deviations of the electric potential from the ideal quadratic potential caused by the holes show a strong dependence on the distance from the trap center (of the order of $z^{22}$), corresponding to a high multipole order, while the symmetry of the end-cap hole arrangement calls for a quadrupole term only. A consequence of this is that the end-cap holes make only a small contribution to the low order terms in the multipole expansion and are “hidden” in a large number of high-order terms. It is possible that for this reason the contribution of the end-cap holes to the electric field in the trap was previously overlooked in studies of the electric field in RF ion traps [45]. However, because the ions have to pass through the end-cap holes during ejection, and since the electric field strength in that region goes from its maximum value to zero, the end-cap holes have an important effect on the ion motion. Since during normal operation of the RF ion trap the ions are confined to positions on or close to the symmetry axis, it is feasible for many problems not to seek the exact multipole expansion for the whole inner volume of the ion trap, but rather to approximate the electric field on the axis only. Using such an approximation, only a small number of multipole terms, one of which is approximately of order 22, are necessary to describe the electric potential. For the case shown in Fig. 3, the expansion was chosen to include three terms: a quadrupole term was chosen to be identical with the quadrupole term of the exact multipole expansion, a second term is used to approximate the potential

deviations in the vicinity of the end-cap holes, and a third term to match the potential in the intermediate region. The expansion coefficients were obtained by manually fitting them to the numerically calculated field values. It was found that on the axis of symmetry the axial electric field in the trap in the theoretical geometry with end-cap holes can be approximated closely by a superposition of $A_6^R/A_2^R = -0.025$ (dodecapole) and $A_{22}^R/A_2^R = -40$ (44-pole). On the axis, the numerically calculated field and the analytical approximation almost coincide except for axial positions larger than $z_0$, where the ions are no longer trapped in any case. The analytical approximation illustrates that no perfect mutual compensation of the field imperfections caused by the end-cap holes and the commercial geometry is possible: while increasing $z_0$ introduces primarily an octopole term, the end-cap holes give rise to the equivalent of a dodecapole and a 44-pole term on the axis of symmetry.

The investigation of the electric field in the trap undertaken here for the Finnigan ITD and ITMS ion traps should be valid also for Finnigan GCQ and LCQ ion traps and Bruker ESQUIRE ion traps. The Finnigan GCQ and LCQ use hyperbolic electrodes that have been shaped according to theory [17] to create a quadrupolar field for an inner ring electrode radius $r_0 = 7.07$ mm and a center–end-cap distance $z_0 = 7.07$ mm. However, as in the Finnigan ITD and ITMS, the center–end-cap distance actually used is $z_0 = 7.83$ mm [16,48]. Calculations show that this geometry gives rise to approximately the same higher order field contributions as the Finnigan ITD and ITMS geometry [29]. Similarly, Bruker ESQUIRE ion traps have been designed to include a similar octopole contribution as the Finnigan ITD and ITMS [40], however using a modified hyperbolic angle rather than an increase in the end-cap separation [18].

### 4.3. Ejection delay and chemical mass shifts

Simulations of the axial ion motion during the mass-selective instability scan with boundary ejection are shown in Fig. 4. Fig. 4a shows the ejection profile for a trap with the theoretical geometry and without end-cap holes. The ejection profile is approximately exponential; rapid ejection of the ion is achieved. Fig. 4b includes the field imperfections due to the end-cap holes. Here, the ion motion shows a significant delay in ion ejection, during which the ion oscillates with very large amplitudes. This motion is very similar to the ejection delay found by Franzen for an ion trap with a negative octopole superposition [49], and it can be explained similarly: after the onset of instability, when the ion secular frequency reaches half the RF frequency, the ion increases its oscillation amplitude by energy uptake from the RF field. Simultaneously with the amplitude increase, its frequency is shifted to lower values due to the sub-linear fields caused by the end-cap holes. As soon as the oscillation frequency is shifted to values below half the RF frequency, the ion motion is stable and the increase in oscillation amplitude stops. The ion is, hence, locked between instability in central regions of the ion trap, and stability in outer regions. It maintains a secular frequency equal to half of the RF frequency. As the RF amplitude is increased, the ion follows an ejection profile with slowly increasing amplitude, until the RF voltage has been increased sufficiently for the ion to reach an oscillation amplitude corresponding to an axial position where the absolute value of the electric field strength decreases with increasing distance from the trap center and the ion is no longer trapped. Following an argument by Franzen [49], in the case of a trap with a negative octopole superposition, the frequency shift is proportional to the square of the oscillation amplitude. The frequency increase due to the scanning of the RF voltage is roughly proportional to the RF amplitude, and hence to time. The requirement to keep the ion secular frequency constant at the boundary, therefore, leads to an increase of the oscillation amplitude approximately with the square-root of the scan time for linear RF scans. In the case of field faults caused by end-cap holes, the oscillation amplitude increases with a higher root because of the stronger dependence of the field strength on position. The sub-structure of the ejection profile, viz. the modulation of the oscillation amplitude reminiscent of a beat motion, is the result of the fact that the ion

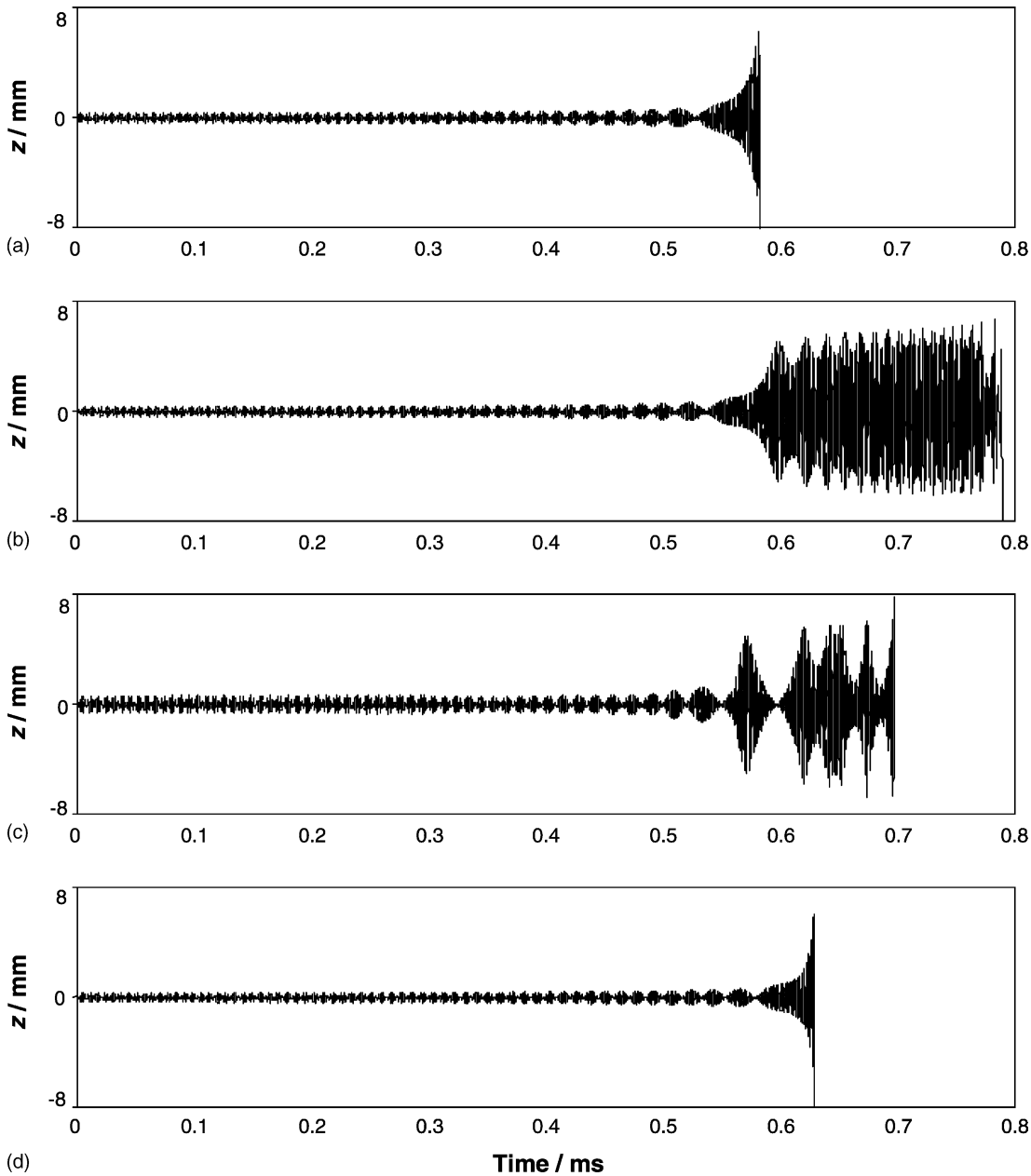


Fig. 4. Simulated ejection profile for boundary ejection of a singly charged ion of mass 100 u in an RF trap with the Finnigan ITMS geometry. The scan rate is 5 Th/ms, the RF frequency is 1 MHz. (a) In the theoretical geometry ($z_0 = 7.07$ mm) without end-cap holes. (b) In the theoretical geometry ($z_0 = 7.07$ mm) with one hole in each end-cap electrode. (c) In the theoretical geometry ($z_0 = 7.07$ mm) with one hole in each end-cap electrode, with elastic collisions with the helium buffer gas. (d) In the commercial geometry ($z_0 = 7.83$ mm) with one hole in each end-cap electrode.

will usually not start the ejection process with the right amplitude for a constant oscillation frequency [49]. It may be located either too close to the center of the trap or to far from the center of the trap. It will, therefore, either rapidly increase its oscillation amplitude or be pushed back. In either case, the motion overshoots and subsequently the oscillation amplitude oscillates around the condition for a constant oscillation frequency. In the following, the term ejection delay will be used to refer to the peculiar motion shown in Fig. 4b, i.e., to the time interval between onset of motional instability in the center of the trap and ion ejection, rather than to a difference in the ion ejection times caused by changing instrumental parameters such as the scan rate.

It should be noted that this ejection delay occurs for all ions, regardless of their mass or chemical structure. A simple calibration would remove the shift in apparent mass caused by the ejection delay, except that the delay is compound-depend due to ion–buffer gas collisions. An example of the effects of such interactions are shown in Fig. 4c. Here, elastic collisions are included in the simulation. Clearly, they tend to shorten the ejection delay. This process is analogous to RF heating due to collisions at stable working points [50]. Collisions change the velocity of the ion, and thus the oscillation phase, and hence may increase or decrease its oscillation amplitude. Both cases destabilize the ion motion during the ejection delay, since the position-dependent frequency shift moves the working point away from the stable oscillation condition, which requires that the secular frequency of the ion is equal to half the RF frequency. As a result, the overshooting effect described before is large, and the ion may be ejected if the overshooting takes it past the axial position of maximum field strength. In the presence of a buffer gas, ions with larger collision cross-sections will tend to be ejected earlier than ions with smaller collision cross-sections.

The effects of elastic collisions on the ion motion shown here differ from those in the work of Sudakov [51] and Cai et al. [52], who report that collisions increase the ejection delay caused by negative higher order fields. This difference is caused by the way the collisions are modeled. The viscous drag model used by Sudakov and Cai et al. continuously removes energy from the ion motion, and thus does not reproduce the oscillation phase shifts required for sudden changes in the oscillation amplitude, which are responsible for the ejection by elastic collisions. Therefore, the viscous drag model is valid only under conditions where the collision frequency is large compared to the frequency of the trapping field. Thus, it can give correct results for the experiments of Cai et al., who investigated large biomolecules in an audio-frequency trap, but for the conditions found in almost all commercial RF ion trap mass spectrometers, collisions have to be treated individually.

An even larger shift in ejection time can arise from inelastic collisions during the ejection delay. The hypothesis that dissociation could play a role in the chemical mass shift was first suggested for *n*-butylbenzene by Londry et al. [53]. While for most of the RF scan the ions oscillate under quasi-thermal conditions with small amplitudes in central regions of the ion trap, during the ejection delay their oscillation amplitudes are large, and in collisions with helium atoms energies in the COM system of several electron volts can occur. This energy is sufficient to excite internal modes of the ion and to cause subsequent dissociation. The fragment ion is of lower mass than the parent ion, so its motion is immediately unstable and it is ejected quickly from the trap. Therefore, fragile ions are ejected (in the form of their fragments) on average earlier than structurally stable ions. Fig. 4 shows that the mass shift associated with ejection delay can be as large as 200 μs for ions of 100 Th. This corresponds to a difference in mass-to-charge ratio of 1 Th, which is of the magnitude of the chemical mass shifts observed in experiments.

An example of the ejection process in a trap in the commercial geometry is shown in Fig. 4d. Since the increase in $z_0$ has removed the negative higher order fields in the inner regions of the ion trap, the ion is ejected rapidly without delay. Thus, the stretch in $z_0$ has compensated for the effects of the field imperfections caused by the end-cap holes, although the

higher order multipole terms do not compensate each other exactly.

Because of the overshooting effect discussed earlier, the length of the ejection delay in the absence of collisions depends strongly on the starting oscillation amplitude and phase. This is evident from the results of simulations of the ejection process with different starting amplitudes [29]. When the initial amplitude is too small, the energy uptake after the onset of instability overshoots, causing a large modulation of the oscillation amplitude, and hence a short ejection delay. When little overshooting occurs long ejection delays are observed. For even larger initial oscillation amplitudes, the overshooting, and hence the modulation of the oscillation amplitude increases again, and the ejection delay is reduced. Note that the early ejection because of large oscillation amplitudes has not been reported previously. An important consequence of this variation in the length of the ejection delay is degradation in mass resolution in addition to poor mass measurement accuracy. Also, the mass resolution and the peak shapes depend on the initial conditions, viz. on the size of the ion cloud at the beginning of motional instability.

The ejection delay is due to an oscillation-amplitude dependent shift of the ion oscillation frequency relative to the frequency required for ejection. For boundary ejection, this critical frequency is the secular frequency at the boundary of the stability diagram. The same frequency argument applies to the mass-selective instability scan with resonance ejection. In this case the critical frequency is the frequency of the resonance voltage. Therefore, the same ejection delay phenomenon should arise for resonance ejection, even though the ejection mechanisms for boundary ejection and resonance ejection are different. This is illustrated in Fig. 5. The conditions for the simulations are the same as in Fig. 4, except that a resonance voltage is applied at a frequency corresponding to $q_z = 0.897$. The resonance ejection profiles differ from the boundary ejection profiles by the additional beat between the resonance excitation frequency and the secular ion frequency (at the beginning of the energy uptake) and the beat between the secular ion frequency and the first sideband frequency (during ion ejection). However, the overall effect is the same, in particular the prolonged ejection delay in the theoretical geometry with end-cap holes, the effect of collisions during the ejection delay, and the removal of the delay in the commercial geometry. For resonance ejection, the onset of the increase in oscillation amplitude is more gradual and longer than for boundary ejection. This is caused by the finite width of the resonance curve. During the initial part of the energy uptake, where the oscillation amplitude increases only slowly, elastic collisions are not very effective in ejecting the ion from the trap, in particular if the working point for resonance ejection is located far from the stability boundary. However, very fragile ions may dissociate in collisions even at these oscillation amplitudes. Therefore, larger chemical mass shifts will be observed for easily dissociating ions for the mass-selective instability scan with resonance ejection than without resonance ejection, and chemical mass shifts caused by elastic collisions will be smaller for resonance ejection than for boundary ejection. Experimental evidence for this is given by Wells et al. [23] and Li et al. [54]. It also explains why small chemical mass shifts were reported by Murphy and Yost [20] for very fragile ions for resonance ejection even in ion traps in the commercial geometry, while no shift was observed for boundary ejection.

### 4.4. Mass dependence of chemical mass shifts

If only the duration of the ejection delay is of interest without consideration of the details of the ion motion itself, the effect of the negative higher order fields can be thought of as an increase $\Delta V$ in the RF amplitude required to eject ions that have experienced the onset of instability at an RF amplitude $V$. The RF amplitude at the time of ion ejection will be $V + \Delta V$. Since the strength of the quadrupolar field and the higher order field contributions both scale linearly with the applied RF amplitude, it follows that the voltage difference $\Delta V$ is proportional to the voltage at the onset of instability $V$

$$\Delta V \propto V \tag{4}$$

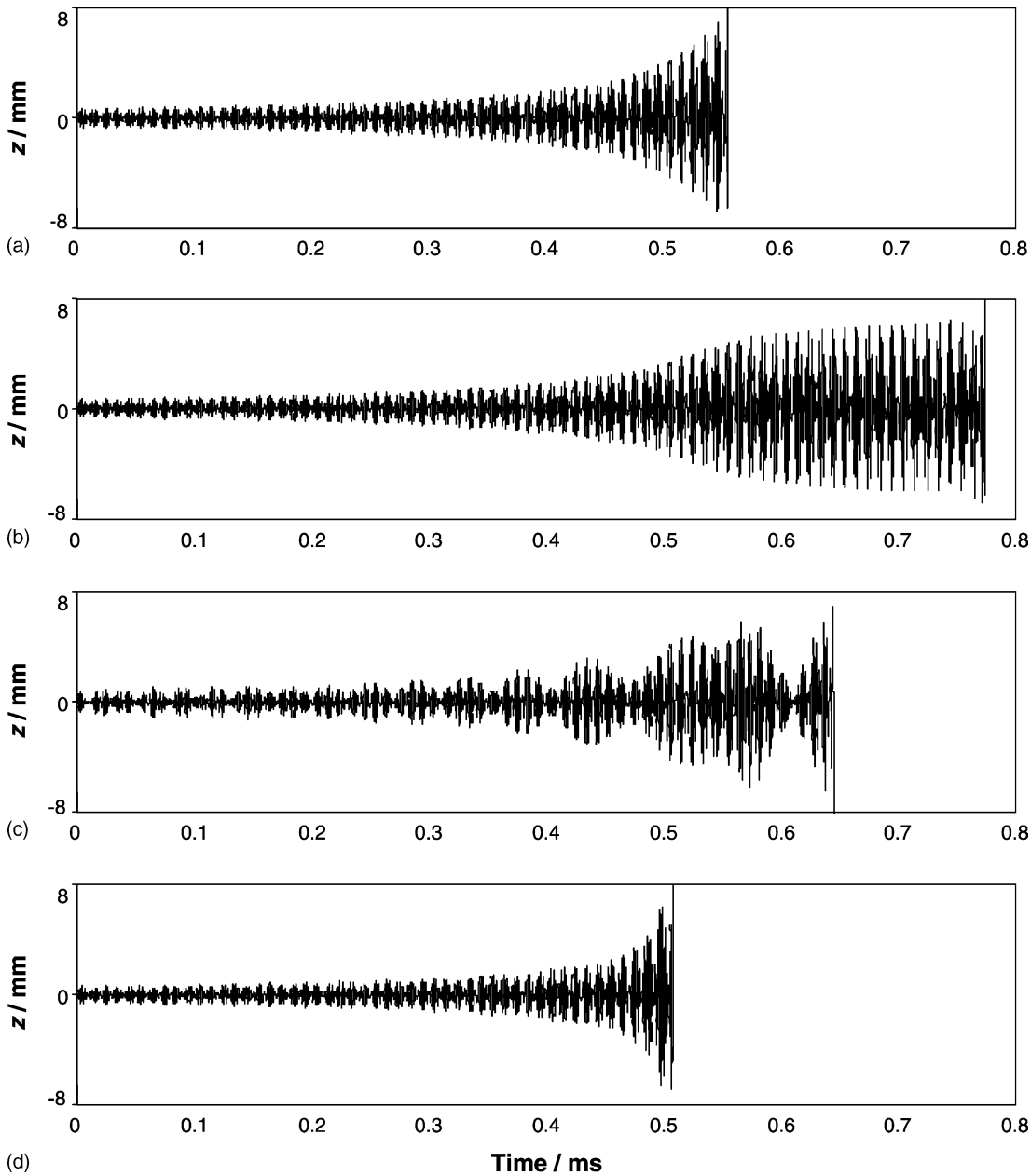


Fig. 5. Simulated ejection profile for resonance ejection of a singly charged ion of mass 100 u in an RF trap with the Finnigan ITMS geometry. The scan rate is 5 Th/ms, the RF frequency is 1 MHz, the resonance frequency 450 kHz and the amplitude 3 V (end-cap–end-cap). (a) In the theoretical geometry ($z_0 = 7.07$ mm) without end-cap holes. (b) In the theoretical geometry ($z_0 = 7.07$ mm) with one hole in each end-cap electrode. (c) In the theoretical geometry ($z_0 = 7.07$ mm) with one hole in each end-cap electrode, with elastic collisions with the helium buffer gas. (d) In the commercial geometry ($z_0 = 7.83$ mm) with one hole in each end-cap electrode.

For the mass-selective instability scan, the mass-to-charge ratio of an ejected ion is proportional to the RF amplitude. Substituting Eq. (1) into Eq. (4), one has for a fixed ejection point $q_z$

$$\left[\Delta\left(\frac{m}{e}\right)\right]_{\max} \propto \frac{m}{e} \tag{5}$$

where $(m/e)$ is the true mass-to-charge ratio of the ion and $[\Delta(m/e)]_{\max}$ the shift in apparent mass-to-charge-ratio caused by the ejection delay in the absence of ion–neutral interactions. In the following, $[\Delta(m/e)]_{\max}$ will be referred to as the maximum ejection delay in order to differentiate it from the shorter ejection delay observed in the presence of ion–neutral interactions. It should be noted, however, that the duration of the ejection delay also depends on the spatial and velocity distribution of the ions at the onset of instability. Therefore, $[\Delta(m/e)]_{\max}$ should be interpreted as an average value for a typical ion ensemble. The relation (7) holds for all ions, regardless of their chemical structure. Thus, the mass shift is not observable in the absence of ion–neutral interactions, provided an appropriate mass calibration is used. Because of different collisional behavior of different ion species, a part of the maximum ejection delay $[\Delta(m/e)]_{\max}$ appears as chemical mass shift. Eq. (5) also holds for the chemical mass shift between two different ion species, provided that a constant fraction of the maximum ejection delay is converted to actual chemical mass shift. This approximation ignores the fact that with increasing ion mass, the collisions with the buffer gas become less effective, and that higher internal energies are required for dissociation. On the other hand, with increasing mass, the kinetic energy of the ions increases. Also, the absolute duration of the ejection delay increases, leaving more time for collisions. These effects can be expected to cancel out approximately.

### 4.5. Scan rate dependence of chemical mass shifts

At a fixed scan rate, the RF amplitude is proportional to the scan time. Following the discussion in the previous section, the time $\Delta t$ required to increase the RF amplitude by the additional amount $\Delta V$ to compensate for the negative higher order fields is, therefore, proportional to $\Delta V$

$$\Delta V = A\Delta t \tag{6}$$

where $\Delta t$ is the duration of the maximum ejection delay. The duration of the ejection delay, thus increases with decreasing scan rate $A$

$$\Delta t \propto A^{-1} \tag{7}$$

However, the shift in mass attributed to the ejection delay stays constant, because according to the mass analysis Eq. (1) the mass conversion also scales with scan rate

$$\left[\Delta\left(\frac{m}{e}\right)\right] \propto A\Delta t \propto A \times A^{-1} = \text{constant} \tag{8}$$

The maximum mass shift that all ions undergo simultaneously in the absence of collisions is, therefore, independent of the scan rate. However, the duration of the ejection delay increases with decreasing scan rate. After a large number of collisions, any ion will be ejected from the trap regardless of its chemical structure. Since the corresponding mass interval decreases with decreasing scan rate, the chemical mass shift will decrease also.

## 5. Quantitative results

### 5.1. Pressure dependence and compound dependence

The ejection times and peak shapes for three different ion species, the 131 u fragment ion of PFTBA, the 134 u isotope of xenon, and the molecular ion of *n*-butylbenzene, were measured using the mass-selective instability scan with boundary ejection in the Finnigan ITMS in the theoretical geometry for different helium buffer gas pressures. These ions were chosen because they are close in mass, and thus allow the focus to fall on their structural differences. PFTBA is a common calibration compound. Xenon was chosen because it is an atom, and thus not subject to dissociation, and because it has a smaller collision cross-section than organic ions. *n*-Butylbenzene is a

common thermometer ion used for gauging internal energies and for investigating dissociation.

The measured peak shapes for the 131 u fragment of PFTBA for three different helium buffer gas pressures are shown in Fig. 6a. At the low pressure of 0.056 mTorr, the peak is shifted to later ejection by about 2 Th and split into four sub-peaks, the last two of which are the most abundant. At this pressure, the ejection process can hardly be influenced by collisions and the peak shapes are determined by the nonlinear fields alone. With increasing pressure the sub-peaks corresponding to the highest apparent mass decrease in abundance, the peak is shifted to earlier ejection, and the peak splitting disappears. This is consistent with the proposed model for the chemical mass shift: without collisions a prolonged ejection delay occurs, and as the number of collisions is increased, the ions are all ejected earlier. However, even at a helium pressure of 0.83 mTorr the ions are still ejected late by about 1 Th.

The measurements can be compared with the simulations shown in Fig. 6b. As discussed earlier, the center–end-cap spacing chosen for the comparison was $z_0 = 6.8$ mm, and the simulated pressures are lower by a factor of two than the experimental value. Using these adjustments, excellent agreement with the experiment is obtained. It should be noted that the peaks belong to one ion species only and that the peak splitting and the peak shift are thus caused by the small field imperfections and the collisions only. The simulations exactly reproduce these effects. The agreement between simulations and experiments shows that the peak splitting observed is a consequence of the ejection delay, and thus establishes the existence of the ejection delay predicted by Franzen [49] for quadrupolar fields with a negative octopole superposition and our earlier simulations for a hyperbolic trap in the theoretical geometry with end-cap holes [22]. The agreement is, thus, a very good indication of the correctness of the proposed chemical mass shift model.

The general change in the peak shapes of the 134 u xenon isotope with an increase in pressure is the same as for PFTBA, but the pressure increase must be approximately twice the pressure increase for PFTBA in order to give rise to the same changes in the peak shapes. This is because the collision cross-section of xenon is about half as large as the collision cross-section of the 131 u fragment ion of PFTBA [29]. The corresponding simulation confirms that the difference in the pressure dependence between PFTBA and xenon is indeed due to the difference in the collision cross-sections.

The measured mass peaks of the molecular ion of *n*-butylbenzene (134 u) at 0.056 mTorr are also very similar to the cases of PFTBA and xenon. However, a small portion of the *n*-butylbenzene ions are ejected earlier, starting at an apparent mass-to-charge ratio of 134.5 Th. As the pressure is increased, this effect becomes much more pronounced. The *n*-butylbenzene peaks are shifted much closer to the theoretical mass-to-charge ratio than either the PFTBA or the xenon peaks. Calculations show that the difference in collision cross-section between PFTBA and xenon is much larger than between PFTBA and *n*-butylbenzene [29]. Thus, elastic collisions cannot account for the differences in the pressure dependence. Dissociation of the molecular ion of *n*-butylbenzene was shown to be the cause by a comparison of the experimental results with the simulations. Inelastic collisions and dissociation of the molecular ion of *n*-butylbenzene were included in these simulations. The average internal energy up-step efficiency for *n*-butylbenzene/helium collisions was chosen as 0.4. This value is consistent with values reported for the conversion efficiency measured in CID experiments on *n*-alkylbenzenes [55].

So far, only shifts of ions of the same species with changes in the buffer gas pressure relative to the case without collisions has been investigated. However, since these shifts are of different magnitude for different ion species, there will also be a chemical mass shift between different ion species for fixed operating conditions. The magnitude of these shifts depends on the buffer gas pressure and is maximized for relatively large pressures. The shifts can be large enough to separate the peaks of ions of the same nominal mass, as shown in Fig. 7a (mass-selective instability scan with boundary ejection in the Finnigan ITMS

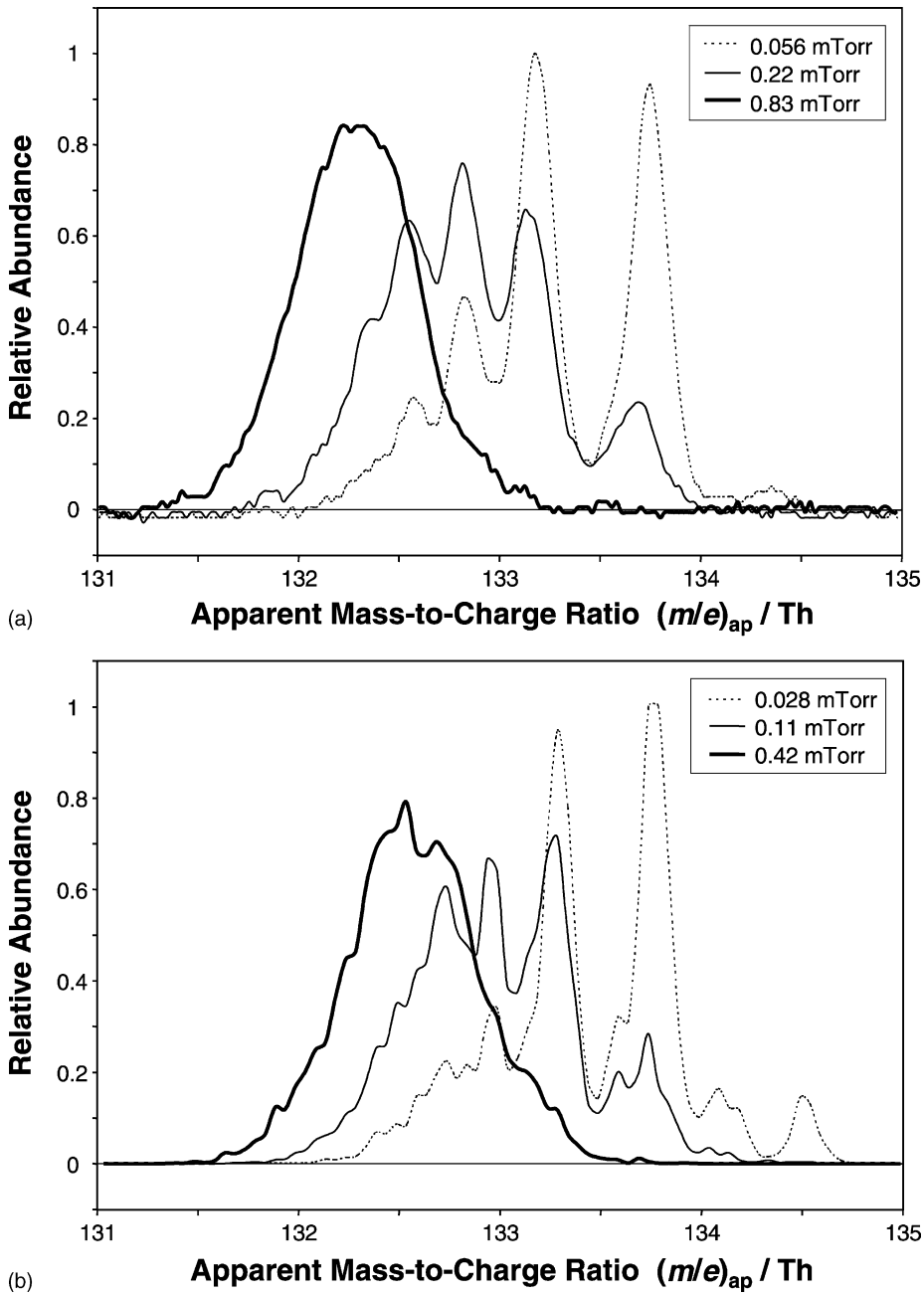


Fig. 6. Boundary ejection peak of the 131 u fragment ion of PFTBA in the Finnigan ITMS ion trap for different helium buffer gas pressures. (a) Experiment with $z_0 = 7.07$ mm. (b) Simulation with $z_0 = 6.8$ mm.

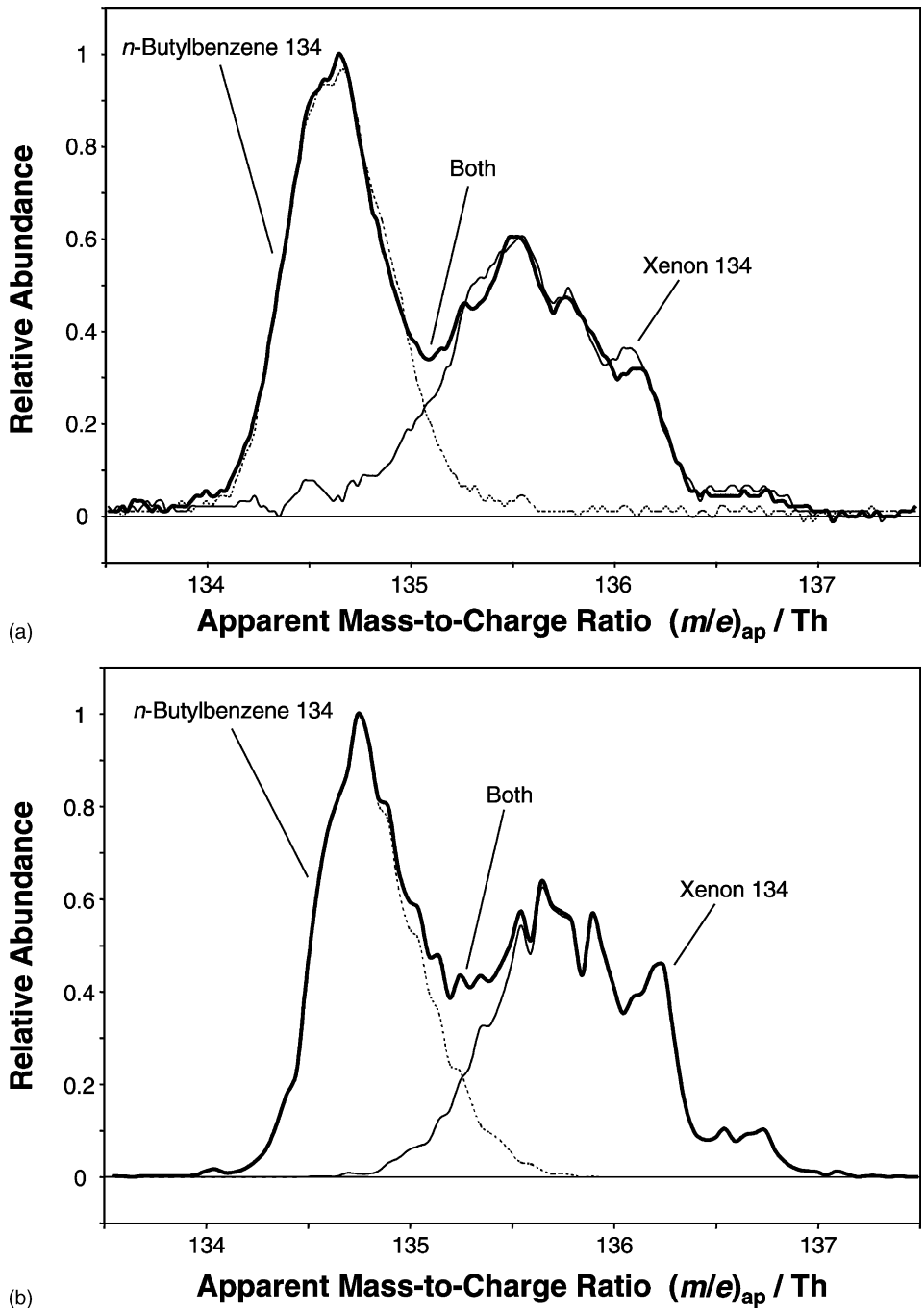


Fig. 7. Resolution of the molecular ion of *n*-butylbenzene (134 u) and the 134 u xenon isotope using chemical shifts by boundary ejection in the Finnigan ITMS ion trap. (a) Experiment with $z_0 = 7.07$ mm and a helium buffer gas pressure of 0.83 mTorr. (b) Simulation with $z_0 = 6.8$ mm and a helium buffer gas pressure of 0.42 mTorr. The thick line shows the abundance when both samples were admitted to the trap, the thin lines the signal of the samples individually.

of the theoretical geometry) for the molecular ion of *n*-butylbenzene (134 u) and the 134 u isotope of xenon. It must be emphasized that the peak separation occurs because of the chemical structure, not because of a mass difference—the exact mass of *n*-butylbenzene is 134.110 u, but it appears at a lower apparent mass than the xenon isotope, which has the exact mass 133.905 u. As comparison and validation, the corresponding simulation is given in Fig. 7b.

The effect of pressure on the positions of the peaks for the 131 u fragment ion of PFTBA, the 134 u isotope of xenon, and the molecular ion of *n*-butylbenzene are given in Fig. 8a in the form of plots of the relative apparent mass, viz. the apparent mass scaled with the theoretically expected mass. As already discussed, the ion ejection point is shifted to earlier times with increasing pressure. The small deviation at very low pressures in the case of xenon is probably due to insufficient cooling after the isolation step, so that the ion cloud sizes at very low pressure were not the same as at other pressures. A larger size of the ion cloud results in fewer ions being ejected late, as discussed earlier. While the effect of elastic collisions on the peak shapes is very important in that it removes peak splitting (Fig. 6), the shifts observed between different non-fragmenting ion species are relatively small. Even for the factor of two difference in collision cross-section between xenon and the 131 u fragment ion of PFTBA, the difference in relative apparent mass is only about 0.002, corresponding to a chemical mass shift of 0.2–0.3 Th. Therefore, chemical mass shifts between organic ions of similar size due to elastic collisions must be very small. Large chemical mass shifts arise as a result of dissociation for the molecular ion of *n*-butylbenzene; its relative apparent mass differs from the 131 u fragment of PFTBA by 0.0065 at higher pressures, corresponding to a chemical mass shift of 0.8–0.9 Th. Simulations (Fig. 8b) confirm these experimental results.

### 5.2. Geometry dependence

The boundary ejection peak shapes of PFTBA for center–end-cap spacings $z_0 = 7.5$, 7.83, and 8.2 mm are shown in Fig. 9 and compared with the corresponding simulations at $z_0 = 7.2$, 7.5, and 8.0 mm. As the center–end-cap spacing is increased, the peak splitting disappears, even at low helium buffer gas pressures, and the peaks become narrower. Also, the peak center is moved closer to the expected mass. For center–end-cap separations of 7.83 mm and larger, the peak center does not shift with the buffer gas pressure, indicating that the chemical mass shift disappears for these center–end-cap separations. This is consistent with the proposed model, since the increase in the end-cap separation compensates for the effect of the end-cap hole field imperfections, and thus removes the ejection delay. At $z_0 = 7.83$ mm, the peaks still show a tailing to higher masses, while at $z_0 = 8.2$ mm the peaks show a tailing to lower mass. Hence, the optimum $z_0$ for the mass-selective instability scan lies between these two values. The simulations exactly reproduce these effects, except that the chemical mass shifts disappear at $z_0 = 7.5$ mm and the optimum in peak shape lies between $z_0 = 7.5$ and 8.0 mm.

The measured peaks at $z_0 = 7.83$ and 8.2 mm have approximately the same width. The change in the peak shapes and peak widths with $z_0$ at smaller values of $z_0$, i.e., the difference between Fig. 6 ($z_0 = 7.07$ mm) and Fig. 9 ($z_0 = 7.5$ mm), is much greater. This may be in part due to the fact that the relative octopole weight introduced by the increase in end-cap separation increases less strongly with increasing $z_0$ and eventually levels off (Fig. 1). However, the observation is in contradiction with measurements made by Gill et al. [25] which showed a minimum for the peak widths for the 131 u fragment ion of PFTBA and the molecular ion of nitrobenzene for $z_0 = 7.7$ mm. When increasing or decreasing $z_0$, the peak width increased; at $z_0 = 7.55$ and 7.85 mm the peak widths were approximately twice as large as the minimum. The discrepancy could perhaps be explained by space charge effects. While the experiments presented here used very low ion abundances and care was taken to keep the ion abundance constant, no such measures were taken in the earlier work. It is probable that a much greater ion abundance was used in their work, giving rise to a significantly wider ion cloud, which

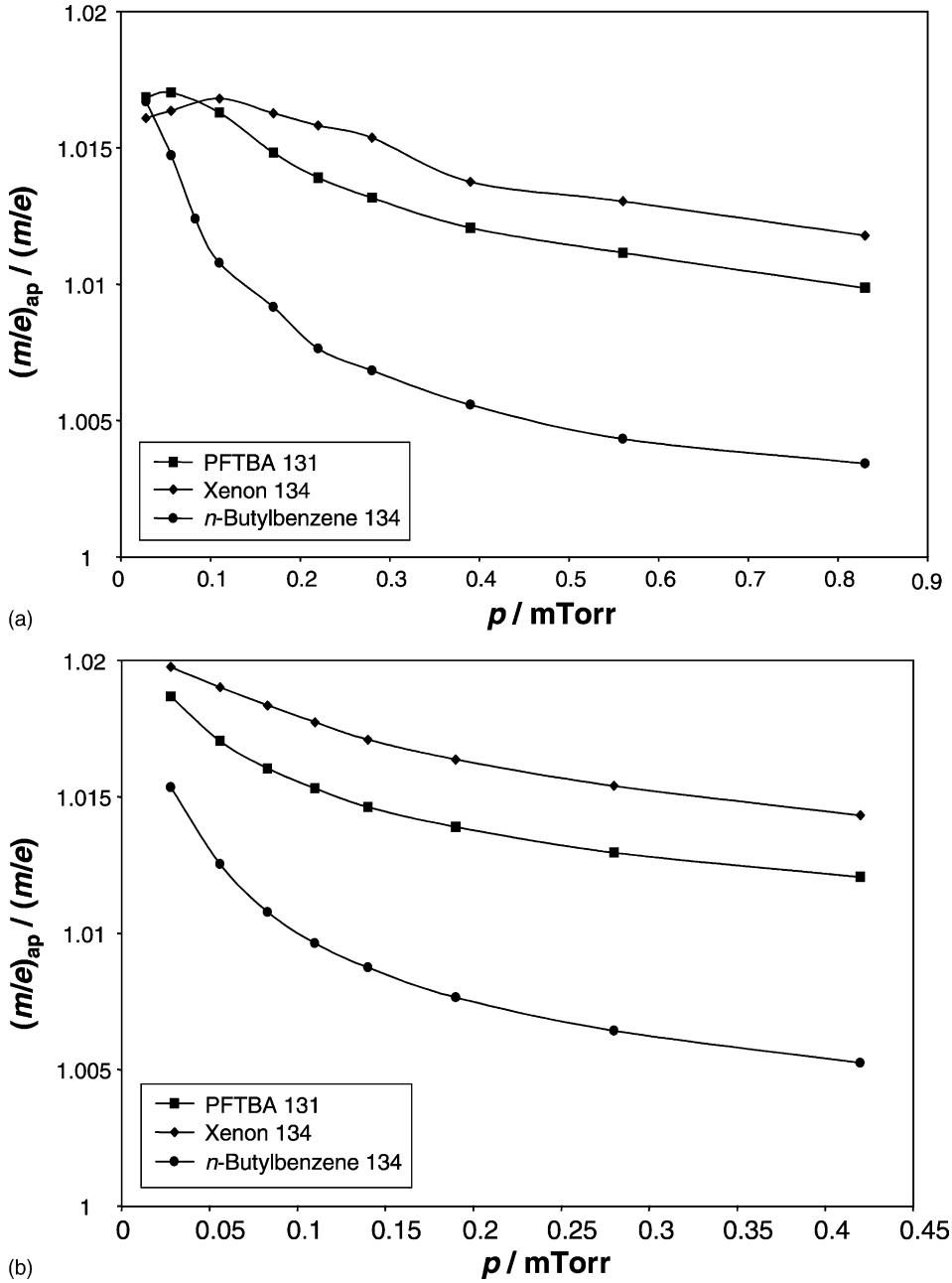


Fig. 8. Dependence of the relative apparent mass of the 131 u fragment ion of PFTBA, the 134 u xenon isotope and the molecular ion of *n*-butylbenzene (134 u) in the Finnigan ITMS ion trap on the helium pressure. (a) Experiment with $z_0 = 7.07$ mm. (b) Simulation with $z_0 = 6.8$ mm.

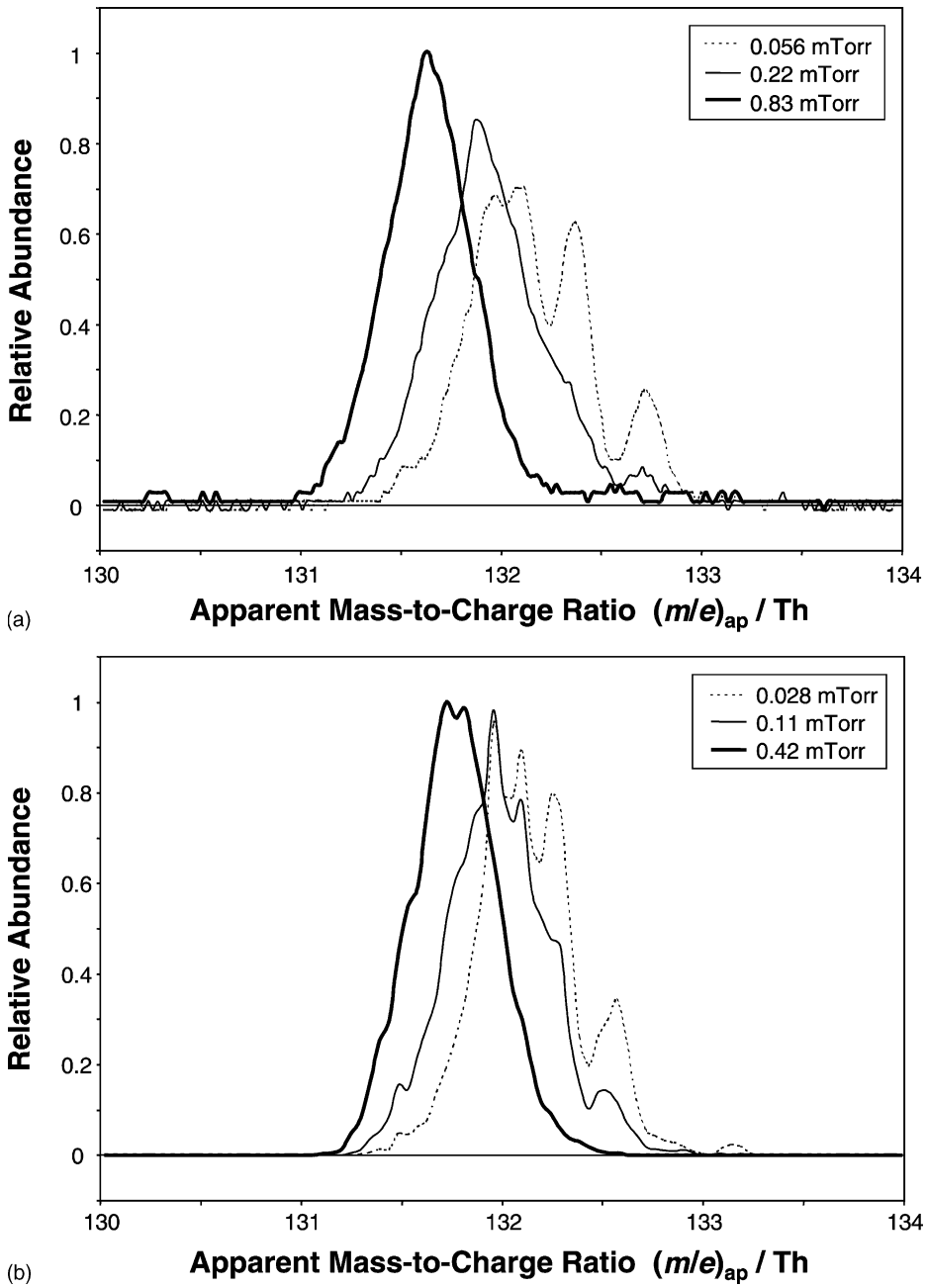


Fig. 9. Boundary ejection peak of the 131 u fragment ion of PFTBA in the Finnigan ITMS ion trap for different helium buffer gas pressures. (a) Experiment with $z_0 = 7.5$ mm. (b) Simulation with $z_0 = 7.2$ mm. (c) Experiment with $z_0 = 7.83$ mm. (d) Simulation with $z_0 = 7.5$ mm. (e) Experiment with $z_0 = 8.2$ mm. (f) Simulation with $z_0 = 8.0$ mm.

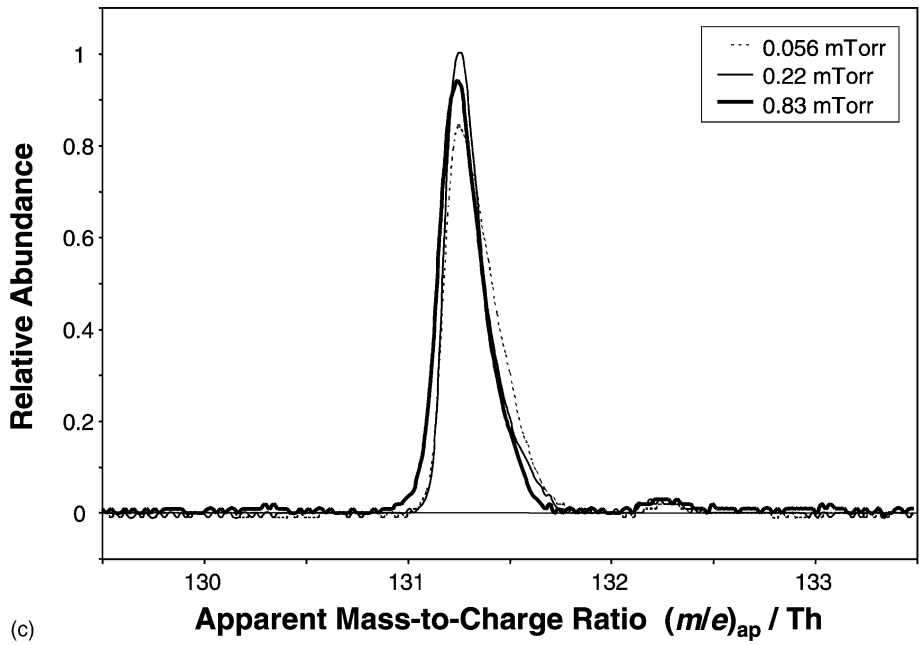


(c)

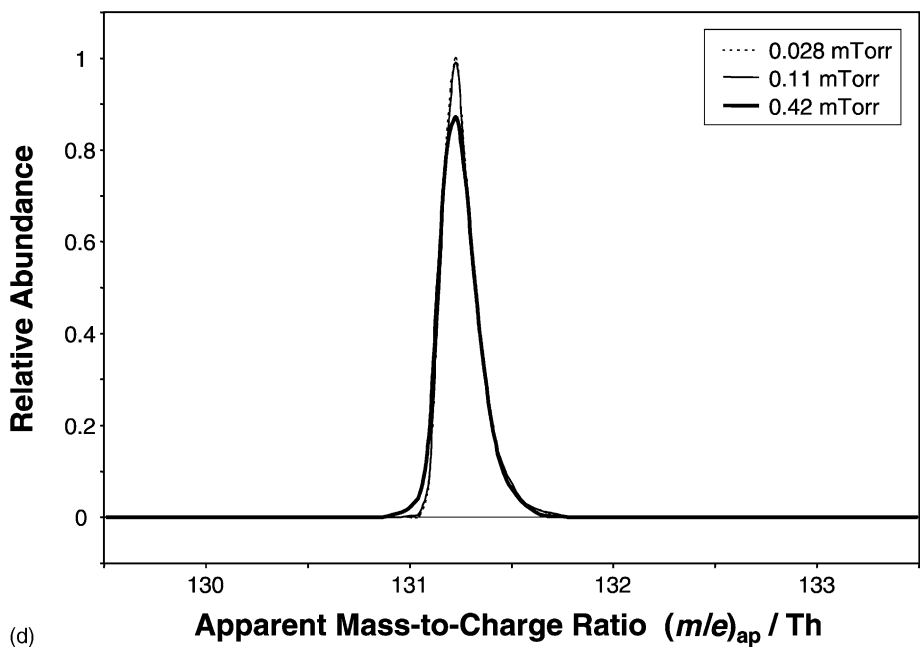


(d)

Fig. 9. (*Continued*).

in turn leads to a much more pronounced effect of the positive higher order field effects of mass resolution. This appears particularly likely since the simulations shown here support the measured peak shapes, but space charge effects were not included in the simulations.

A summary of the measured and simulated dependence of the relative apparent mass on $z_0$ is given for

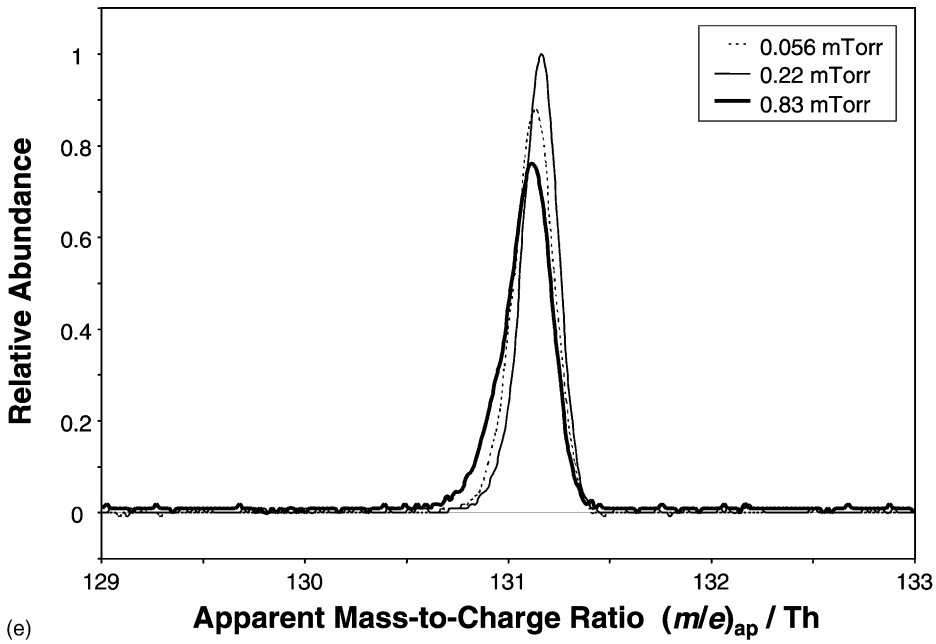


(e)

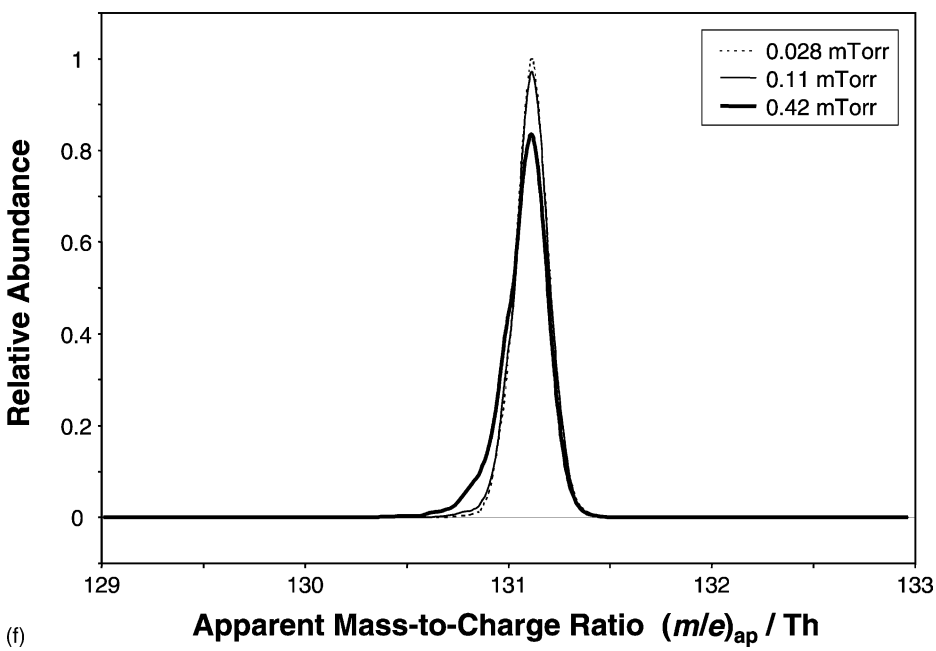


(f)

Fig. 9. (*Continued*).

all three investigated ion species in Fig. 10. At $z_0 = 7.07$ mm (experiment) and $z_0 = 6.8$ mm (simulation), in particular at low pressures, the apparent mass is larger than the true mass (by a factor of 1.005–1.02) and this difference is due to the ejection delay. The apparent mass decreases almost linearly with increasing $z_0$, and so does the chemical mass shift between different compounds. The chemical mass shift disappears

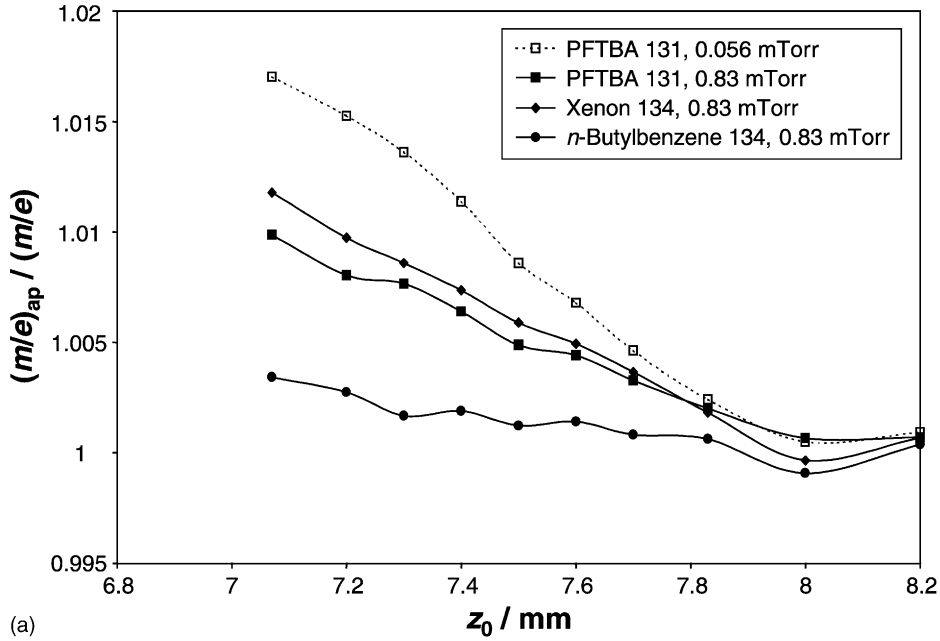


(a)

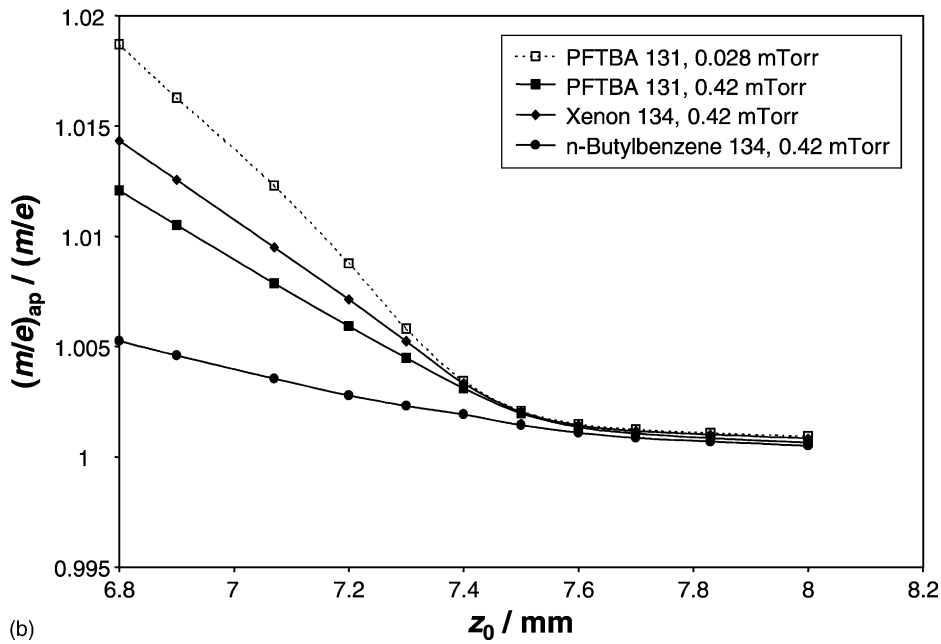


(b)

Fig. 10. Dependence of the relative apparent mass of the of the 131 u fragment ion of PFTBA, the 134 u xenon isotope and the molecular ion of *n*-butylbenzene (134 u) in the Finnigan ITMS ion trap on $z_0$. (a) Experiment. (b) Simulation.

in the commercial geometry at $z_0 = 7.83$ mm (experiment) and $z_0 = 7.5$ mm (simulation). It is interesting to note that the $z_0$ value for an optimum peak shape (vide supra) is slightly larger that the $z_0$ value for which the mass shift starts to vanish. For larger values of $z_0$, the chemical mass shift is zero, and the relative apparent mass is close to the theoretically expected value and does not change significantly with $z_0$. This also justifies matching the simulated and measured scan rates at $z_0 = 8.0$ mm, since there deviations in $z_0$ do not influence the results significantly. Apart from the shift in $z_0$ between experiment and simulation, the results match very well. It should be noted that the ejection delay is visible in Fig. 10 only because of the conversion to apparent mass by Eq. (1), which removes the effect of the change in (quadrupolar) field strength caused by the change in the end-cap separation. The change in ejection time because of the field strength change is larger by an order of magnitude than the change because of nonlinear field effects. Thus, in plots in which the uncorrected ejection time is shown, the ejection delay is hidden and the ejection time decreases with increasing end-cap separation [25].

The difference in the $z_0$ value required to get the same results in the experiment and in the simulations could be explained by deviations between the real and the modeled geometry. The error associated with the measurement of the center–end-cap separation is believed to be less than 0.1 mm, and thus smaller than the shift of 0.3 mm. Also, independent measurements at Finnigan show that chemical mass shifts are still present at $z_0 = 7.58$ mm, while they disappear at $z_0 = 7.83$ mm [16]. This is consistent with the measurements given here. The $z_0$ measurement is, therefore, probably not at fault. Additional errors could arise from possible deviations of the electrodes from the hyperbolic shape and from different end-cap hole diameters and hole shapes. The field faults introduced by the end-cap holes approximately scale with the cube of the hole diameter [56]. Hence, small differences in the end-cap hole size and shape have a strong impact on the ion motion and on the chemical mass shift. It is also possible that penetration of electric fields, e.g., from the ion source and the detector, occurs in real ion traps, which has not been included in the field calculations. Other influences on the ion motion that are ignored in the simulations, such as ion–ion interactions, may play a role. It is unlikely, however, that specific ion–neutral collision mechanisms are of importance, since the chemical mass shifts of xenon and *n*-butylbenzene, which should differ significantly in their collisional behavior, vanish at the same $z_0$ value.

### 5.3. Mass dependence

The linear dependence of the maximum ejection delay on the ion mass derived in Section 4.4 has been verified in simulations which are not shown here. The experimental validation of the linear dependence of the chemical mass shift on ion mass is difficult, because it would require the investigation of ions that differ significantly in their mass, but have identical chemical properties. However, several studies [57,58] have shown that the best correlation of the chemical mass shifts with the ease of fragmentation of the investigated ions is found if the relative chemical mass shift $\Delta(m/e)/(m/e)$ is considered, which corrects for the mass dependence. In addition, published values [22] of chemical mass shifts show that the maximum shifts observed in the Finnigan ITMS in the theoretical geometry is approximately $\Delta(m/e) = 0.0065(m/e)$, and hence increase linearly with mass. This maximum shift occurs for ions that are sufficiently fragile to dissociate already at the beginning of the ejection delay.

### 5.4. Scan rate dependence

The chemical mass shifts of the molecular ion of nitrobenzene were measured in the Finnigan ITMS as a function of the scan rate attenuation factor using a custom RF-DAC attenuator circuit [59]. The results are in accordance with the prediction (Section 4.5): for a constant pressure, the chemical mass shift decreases slowly with decreasing scan rate. While the maximum ejection delay, measured in mass units, is independent of the scan rate, the longer duration—in time units—allows for more collisions to occur over the same mass interval. As the scan rate is increased,

both the nitrobenzene ions and the PFTBA calibrant ions are ejected earlier in the ejection delay, reducing the chemical mass shift.

### 5.5. Shifts to higher apparent mass

So far it has been shown that chemical mass shifts can be large for fragile ions. Chemical mass shifts because of elastic scattering are small and can probably be neglected except for ions of very different collision cross-sections. Assuming that the calibrant ions are structurally stable and do not dissociate during the ejection delay, only chemical mass shifts to lower apparent mass—relative to the calibrant ions—can occur. Using the definition given earlier, they are positive.

However, the mass shift measurements observed during the development of the mass-selective instability scan at Finnigan using an ion trap mass spectrometer in the theoretical geometry were to both lower and to higher apparent mass, depending on the ion species [16]. In particular, the molecular ions of pyrene, anthracene and the 223 u fragment ion of hexachlorobutadiene were reported to have chemical mass shifts between 0.5 and 0.7 Th to higher apparent mass. These ions are relatively stable to fragmentation and do not have significantly smaller collision cross-sections than the calibrant ions. A possible explanation is that the calibrant ions, fragment ions of PFTBA, themselves were subject to dissociation during the ejection delay, and that, relative to the calibrant ions, the mentioned ions were assigned a shift to higher apparent mass.

To test this hypothesis, the chemical mass shifts of the ions mentioned were measured in the Finnigan GCQ mass spectrometer in the theoretical geometry. The instrument was calibrated using the 69, 100, and 131 u fragment ions of PFTBA. The results are shown

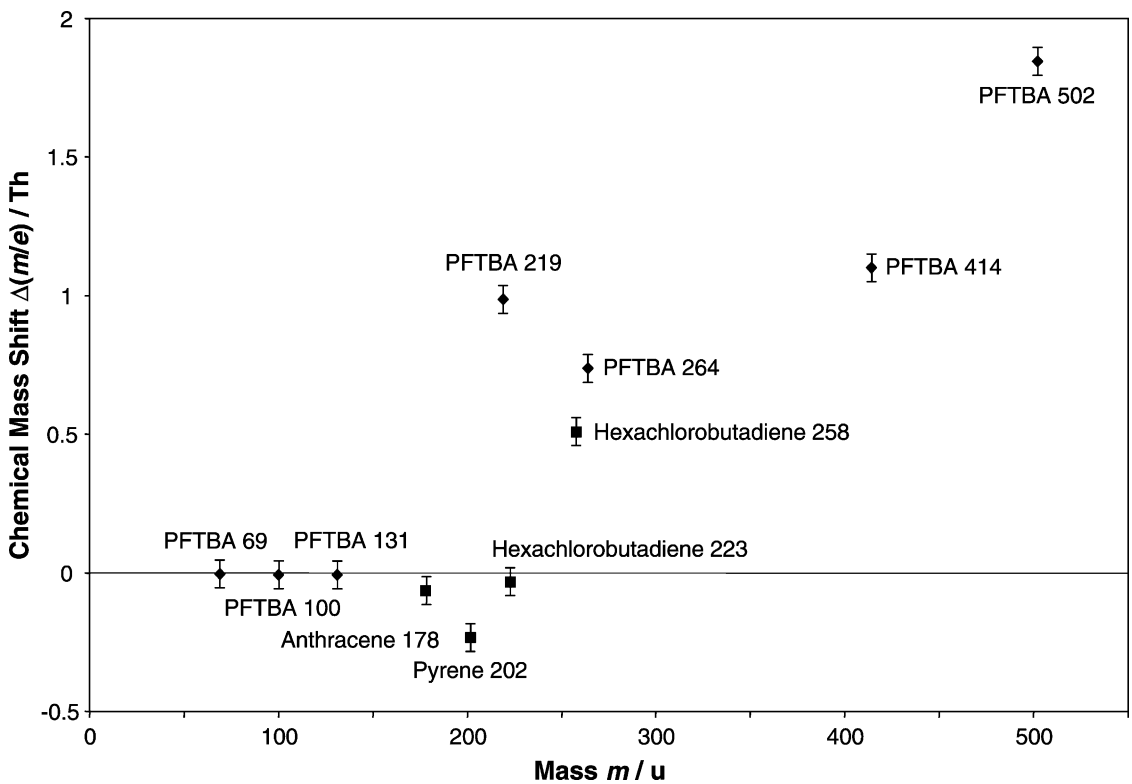


Fig. 11. Chemical mass shift of high mass PFTBA fragment ions and other organic ions relative to the 69, 100, and 131 u fragment ions of PFTBA measured using boundary ejection in the Finnigan GCQ ion trap with $z_0 = 7.07$ mm.

in Fig. 11. From the data, it is clear that relative to the low mass ions of PFTBA the investigated high mass ions of the same compound show large chemical mass shifts, even taking into account the fact that extrapolation of the calibration line from the mass range 69–131 u to a mass of 500 u may be questionable. On average, the shift of the investigated high mass PFTBA fragment ions increases with mass. It can thus be assumed that these ions do indeed undergo fragmentation during the ejection delay. Care should be taken when using these ions as calibrant ions. Whether dissociation of the high-mass PFTBA ions occurs to a small extent even in the commercial geometry has not been investigated.

Relative to the low mass fragment ions of PFTBA, anthracene and the 223 u fragment ion of hexachlorobutadiene do not exhibit a substantial mass shift. Why the molecular ion of pyrene shows a small negative chemical shift, i.e., a shift to higher apparent mass, even in these measurements, is currently not understood. Particularly instructive is the case of the molecular ion of hexachlorobutadiene, which had been reported to exhibit no mass shift [16]. Here it is shown to shift by about 0.5 Th to lower apparent mass, while its fragment ion of 223 u does not shift. Thus, the same mass shift between the molecular ion of hexachlorobutadiene and its 223 u fragment ion is obtained as the one reported by Syka, but here it is attributed to the molecular ion, which is more likely to undergo fragmentation.

## 6. Conclusions

Chemical mass shifts which can arise in ion traps with non-optimized geometry have been examined. They are shown to be caused by a prolonged delay in ion ejection due to field imperfections in the vicinity of the end-cap holes, which is modified in a compound-dependent fashion by collisions of the ions with the buffer gas. Elastic collisions shorten the ejection delay for all ions and remove the characteristic peak splitting caused by nonlinear field components. Since differences in collision cross-sections for ions of similar masses are typically small, the change in ejection delay is similar for ions of similar mass, so elastic collisions can give rise to only very small chemical mass shifts. Large chemical mass shifts are caused by the dissociation of polyatomic ions during the ejection delay. Introduction of a small amount of positive higher order fields can offset the effect of the field imperfections and remove the ejection delay for all ions, and hence the chemical mass shift. The dependence on the operating conditions (trap geometry, pressure, ion mass and chemical properties of the ions) and additional effects connected with chemical mass shifts (shifts to higher apparent mass, differences between boundary ejection, and resonance ejection) are all explained in this work.

Ion traps are usually designed to exclude chemical mass shifts. However, chemical mass shifts could also be of advantage. Since ions can be separated based on their shifts, even isomeric ions can be distinguished [60]. By proper choice of the operating conditions chemical mass shifts can be enhanced or switched off, and provided two peaks are resolved they can be separated by an arbitrarily large time using an appropriate scan function [61]. A further application of chemical mass shifts might be the investigation or measurement of chemical properties of ions that are related with their ease of dissociation, such as internal energy transfer characteristics, as indicated here, or substituent effects [57].

The quantitative investigation of the nonlinear fields in the hyperbolic ion trap that has been presented here should be useful in the design of RF traps, including variant geometries such cylindrical traps [62] and linear traps [63]. It has been shown that in the inner regions of commercial ion traps positive nonlinear fields are present, while in the outer regions on the axis of symmetry negative nonlinear fields dominate. These two regimes are caused (i) by the field imperfections introduced by the end-cap holes and to a lesser degree perhaps by other imperfections, such as the truncation of the electrodes, and (ii) intentional changes in the trap geometry such as an increased end-cap electrode separation or a modified hyperbolic angle. The present findings of a compensation of negative and positive

higher order fields in the optimum trap geometry stand in contrast to the widespread opinion that a substantial amount of positive higher order fields are advantageous for the mass-selective instability scan. While positive higher order fields can sharpen the ejection process for an individual ion, they also introduce an oscillation amplitude dependence of the ejection time which increases the time-span over which a group of ions of the same mass-to-charge ratio is ejected, giving rise to broader peaks. Further simulations show that for the mass-selective instability scan with boundary ejection best results are obtained in purely linear fields, and that higher order fields of both signs are detrimental [29].

Since the higher order fields caused by the end-cap holes and the increase in the end-cap separation or the modified hyperbolic angle are not of the same order, they cannot be used for perfect mutual compensation; only approximate compensation of their effects is possible. An RF ion trap mass spectrometer with a geometry that corrects for the field imperfections caused by the end-cap holes by local changes in the field in vicinity of the end-cap holes [64] instead by a global change in the trap geometry could lead to better RF ion trap performance, because it does not contain far-reaching, global higher order fields. For example, nonlinear resonances could be reduced, and with them unwanted ion loss for certain operating parameters.

The mass calibration method used here by application of Eq. (1) was shown to be very useful in investigating nonlinear field effects, since it relies on instrumental parameters only and does not require calibrant ions. It is, hence, independent from the behavior of the calibrants and is able to show absolute effects that are otherwise hidden because both analyte and calibrants are subject to them.

The quality of the simulations shown here for the validation of the chemical mass shift model far surpasses that of any RF ion trap mass scan simulation published before. However, very good agreement with the experiments is only achieved if experimental and simulated geometries differ slightly in the end-cap separation, indicating that additional previously neglected field imperfections may be present in common RF ion traps. Two points should be emphasized: (i) For the first time has it been shown that physico-chemical properties of ions in the RF ion trap can be modeled accurately, beyond the point charge approximation and simple collision models. Thus, it should also be possible to investigate—in addition to mass resolution and mass measurement accuracy—important applications, such as the collision-induced dissociation of ions in the RF ion trap. (ii) It has been demonstrated that peak shapes of mass spectra can be predicted and reproduced accurately in ion trap simulations. Previously ion trap simulations had mostly concentrated on the investigation of individual ion trajectories that cannot be compared easily with experiments. However, the types of simulations of peak shapes shown here can be compared directly with the mass spectra acquired in any RF ion trap mass spectrometer. This makes it possible to explore unexplained effects by a simple comparison of simulation and experiment.

## Acknowledgements

This work was supported by the US Department of Energy, Office of Basic Sciences (Contract DE-FG02-94ER14470) and the Thermo Finnigan Corp. through the Purdue University Industrial Associates Program. The authors thank J.M. Wells and G.E. Patterson for help with the instruments, A.E. Counterman and D.E. Clemmer for the cross-section calculations, P.W. Thomas for fruitful discussions and R. Replogle for precision machining.

## References

[1] G.C. Stafford, P.E. Kelley, J.E.P. Syka, W.E. Reynolds, J.F.J. Todd, Int. J. Mass Spectrom. Ion Process. 60 (1984) 85.
[2] G.C. Stafford, P.E. Kelley, D.R. Stephens, US Patent No. 4,540,884 (1985).
[3] R.E. Kaiser, R.G. Cooks, J. Moss, P.H. Hemberger, Rapid Commun. Mass Spectrom. 3 (1989) 50.
[4] D.B. Tucker, C.H. Hameister, S.C. Bradshaw, D.J. Hoekman, M. Weber-Grabau, Proceedings of the 36th ASMS Conference on Mass Spectrometry and Allied Topics, San Francisco, CA, 1988, p. 628.
[5] J.V. Johnson, R.A. Yost, P.E. Kelley, D.C. Bradford, Anal. Chem. 62 (1990) 2162.

[6] W.E. Pereira, C.E. Rostad, T.J. Leiker, Anal. Chim. Acta 228 (1990) 69.
[7] I. Horman, H. Traitler, J. Aeschlimann, J. High Resolut. Chromatogr. 12 (1989) 308.
[8] G.L. Glish, S.A. McLuckey, K.G. Asano, J. Am. Soc. Mass Spectrom. 1 (1990) 166.
[9] J.N. Louris, R.G. Cooks, J.E.P. Syka, P.E. Kelley, G.C. Stafford, J.F.J. Todd, Anal. Chem. 59 (1987) 1677.
[10] J.N. Louris, J.S. Brodbelt-Lustig, R.G. Cooks, G.L. Glish, G.J. VanBerkel, S.A. McLuckey, Int. J. Mass Spectrom. Ion Process. 96 (1990) 117.
[11] R.G. Cooks, A.L. Rockwood, Rapid Commun. Mass Spectrom. 5 (1991) 93.
[12] J.M. Wells, L.A. Gill, Z. Ouyang, G.E. Patterson, W. Plass, E.R. Badman, J.W. Amy, R.G. Cooks, J.C. Schwartz, G.C. Stafford, M.W. Senko, Proceedings of the 46th ASMS Conference on Mass Spectrometry and Allied Topics, Orlando, FL, May 31–June 4, 1998, p. 485.
[13] J.C. Schwartz, T.A. Hememway, Proceedings of the 48th ASMS Conference on Mass Spectrometry and Allied Topics, Long Beach, CA, 2000, p. MPB 070.
[14] K.A. Cox, C.D. Cleven, R.G. Cooks, Int. J. Mass Spectrom. Ion Process. 144 (1995) 47.
[15] H.A. Bui, R.G. Cooks, J. Mass Spectrom. 33 (1998) 297.
[16] J.E.P. Syka, in: R.E. March, J.F.J. Todd (Eds.), Practical Aspects of Ion Trap Mass Spectrometry, vol. 1, CRC Press, Boca Raton, FL, 1995, p. 169.
[17] R.D. Knight, Int. J. Mass Spectrom. Ion Phys. 51 (1983) 127.
[18] J. Franzen, R. Gabling, G. Heinen, G. Weiss, US Patent No. 4,882,484 (1989).
[19] R.W. Vachet, J.A.R. Hartman, J.H. Callahan, J. Mass Spectrom. 33 (1998) 1209.
[20] J.P. Murphy III, R.A. Yost, Rapid Commun. Mass Spectrom. 14 (2000) 270.
[21] J.E. McClellan, J.P. Murphy III, J.J. Mulholland, R.A. Yost, Anal. Chem. 74 (2002) 402.
[22] J.M. Wells, W.R. Plass, G.E. Patterson, Z. Ouyang, E.R. Badman, R.G. Cooks, Anal. Chem. 71 (1999) 3405.
[23] J.M. Wells, W.R. Plass, R.G. Cooks, Anal. Chem. 72 (2000) 2677.
[24] W.R. Plass, J.M. Wells, R.G. Cooks, Proceedings of the 48th ASMS Conference on Mass Spectrometry and Allied Topics, Long Beach, CA, June 11–15, 2000.
[25] L.A. Gill, J.W. Amy, W.E. Vaughn, R.G. Cooks, Int. J. Mass Spectrom. 188 (1999) 87.
[26] R.L. Summers, NASA Technical Note TN D-5285, National Aeronautics and Space Administration, Washington, DC, June 1969.
[27] R.E. March, F.A. Londry, in: R.E. March, J.F.J. Todd (Eds.), Practical Aspects of Ion Trap Mass Spectrometry, vol. 1, CRC Press, Boca Raton, FL, 1995, p. 25.
[28] W.R. Plass, L.A. Gill, H.A. Bui, R.G. Cooks, J. Phys. Chem. 104 (2000) 5059.
[29] W.R. Plass, Ph.D. Thesis, Justus-Liebig-Universität Giessen, Germany, 2001.
[30] J.H. Billen, L.M. Young, Proceedings of the 1993 Particle Accelerator Conference, 1993, p. 790.
[31] H.W. Ellis, M.G. Thackston, E.W. McDaniel, E.A. Mason, At. Data Nucl. Data Tables 31 (1984) 113.
[32] L.A. Viehland, E.A. Mason, At. Data Nucl. Data Tables 60 (1995) 37.
[33] S.C. Henderson, J. Li, A.E. Counterman, D.E. Clemmer, J. Phys. Chem. B 103 (1999) 8780.
[34] W.R. Plass, R.G. Cooks, J. Am. Soc. Mass Spectrom., in press.
[35] R.G. Gilbert, S.C. Smith, Theory of Unimolecular and Recombination Reactions, Blackwell Scientific Publications, Oxford, 1990.
[36] T. Baer, O. Dutuit, H. Mestdagh, C. Rolando, J. Phys. Chem. 92 (1988) 5674.
[37] D.J. Jackson, Classical Electrodynamics, Wiley, New York, 1975.
[38] W.R. Plass, Int. J. Mass Spectrom. 202 (2000) 175.
[39] N.W. McLachlan, Theory and Applications of Mathieu Equations, Oxford University Press, Oxford, 1947.
[40] J. Franzen, R.H. Gabling, M. Schubert, Y. Wang, in: R.E. March, J.F.J. Todd (Eds.), Practical Aspects of Ion Trap Mass Spectrometry, vol. 1, CRC Press, Boca Raton, FL, 1995, p. 49.
[41] J.D. Williams, K.A. Cox, R.G. Cooks, S.A. McLuckey, K.J. Hart, D.E. Goeringer, Anal. Chem. 66 (1994) 725.
[42] A.A. Makarov, Anal. Chem. 68 (1996) 4257.
[43] P.H. Dawson, N.R. Whetten, Int. J. Mass Spectrom. Ion Phys. 2 (1969) 45.
[44] Y. Wang, Rapid Commun. Mass Spectrom. 7 (1993) 920.
[45] Y. Wang, J. Franzen, Int. J. Mass Spectrom. Ion Process. 132 (1994) 155.
[46] J.M. Wells, Ph.D. Thesis, Purdue University, West Lafayette, USA, 2000.
[47] C.D. Cleven, R.G. Cooks, A.W. Garrett, N.S. Nogar, P.H. Hemberger, J. Phys. Chem. 100 (1996) 40.
[48] J. Louris, J. Schwartz, G. Stafford, J. Syka, D. Taylor, Proceedings of the 40th ASMS Conference on Mass Spectrometry and Allied Topics, Washington, DC, 1992, p. 1003.
[49] J. Franzen, Int. J. Mass Spectrom. Ion Process. 125 (1993) 165.
[50] F.G. Major, H.G. Dehmelt, Phys. Rev. 170 (1968) 91.
[51] M. Sudakov, Int. J. Mass Spectrom. 206 (2001) 27.
[52] Y. Cai, W.-P. Peng, S.-J. Kuo, H.-C. Chang, Int. J. Mass Spectrom. 214 (2002) 63.
[53] F.A. Londry, R.J.S. Morrison, R.E. March, Proceedings of the 43rd ASMS Conference on Mass Spectrometry and Allied Topics, Atlanta, GA, 1995, p. 1124.
[54] H. Li, W.R. Plass, G.E. Patterson, R.G. Cooks, J. Mass Spectrom. 37 (2002) 1051.
[55] S. Nacson, A.G. Harrison, Int. J. Mass Spectrom. Ion Process. 63 (1985) 325.
[56] L.S. Brown, G. Gabrielse, Rev. Mod. Phys. 58 (1986) 233.
[57] Y. Peng, W.R. Plass, R.G. Cooks, J. Am. Soc. Mass Spectrom. 13 (2002) 623.
[58] H. Li, Y. Peng, W.R. Plass, R.G. Cooks, Int. J. Mass Spectrom. 222 (2003) 481.
[59] R.E. Kaiser, R.G. Cooks, G.C. Stafford, J.E.P. Syka, P.H. Hemberger, Int. J. Mass Spectrom. Ion Process. 106 (1991) 79.

[60] L.A. Gill, J.M. Wells, G.E. Patterson, J.W. Amy, R.G. Cooks, Anal. Chem. 70 (1998) 4448.
[61] H. Li, W.R. Plass, R.G. Cooks, Proceedings of the 50th ASMS Conference on Mass Spectrometry and Allied Topics, Orlando, FL, June 2–7, 2002.
[62] E.R. Badman, R.C. Johnson, W.R. Plass, R.G. Cooks, Anal. Chem. 70 (1998) 4896.
[63] J.C. Schwartz, M.W. Senko, J.E. Syka, J. Am. Soc. Mass Spectrom. 13 (2002) 659.
[64] E. Kawato, US Patent No. 6,087,658 (2000).